DOI: 10.1016/j.jconrel.2023.01.047

Delivery of macromolecules in unstimulated T cells by photoporation with polydopamine nanoparticles

Dominika Berdecka [a,b], Aranit Harizaj [a], Ilia Goemaere [a,b], Deep Punj [a], Glenn Goetgeluk [c], Stijn De Munter [c], Herlinde De Keersmaecker [a,d], Veerle Boterberg [e], Peter Dubruel [e], Bart Vandekerckhove [c], Stefaan C. De Smedt [a], Winnok H. De Vos [b, #] and Kevin Braeckmans [a,d,#,*]

[a] Laboratory of General Biochemistry and Physical Pharmacy, Faculty of Pharmaceutical Sciences, Ghent University, Ottergemsesteenweg 460, 9000 Ghent, Belgium

[b] Laboratory of Cell Biology and Histology, Department of Veterinary Sciences, University of Antwerp, Universiteitsplein 1, 2610 Wilrijk, Belgium

[c] Department of Diagnostic Sciences, Faculty of Medicine and Health Sciences, Ghent University Hospital, Heymanslaan 10, 9000 Ghent, Belgium

[d] Ghent Light Microscopy Core, Ghent University, 9000 Ghent, Belgium

[e] Polymer Chemistry and Biomaterials Group, Department of Organic and Macromolecular Chemistry, Ghent University, Krijgslaan 281, 9000 Ghent, Belgium

[#]Shared senior authorship

*Correspondence: Kevin.Braeckmans@ugent.be; Tel.: +32-9-2648098; Fax: +32-9-2648189

Keywords: T cells, polydopamine nanoparticles, photoporation, intracellular delivery, cell therapy

List of abbreviations

AuNPs	Gold nanoparticles
BSA	Bovine serum albumin
CAR	Chimeric antigen receptor
DPBS	Dulbecco's phosphate buffered saline
DLS	Dynamic light scattering
FD500	FITC-dextran 500 kDa
FITC	Fluorescein isothiocyanate
IFN	Interferon
NPs	Nanoparticles
NTA	Nanoparticle tracking analysis
PBMCs	Peripheral blood mononuclear cells
PDNPs	Polydopamine nanoparticles
SEM	Scanning electron microscopy
TCR	T cell receptor
TNF	Tumor necrosis factor
VNBs	Vapor nanobubbles

Abstract

Ex vivo modification of T cells with exogenous cargo is a common prerequisite for the development of T cell therapies, such as chimeric antigen receptor therapy. Despite the clinical success and FDA approval of several such products, T cell manufacturing presents unique challenges related to therapeutic efficacy after adoptive cell transfer and several drawbacks of viral transduction-based manufacturing, such as high cost and safety concerns. To generate cellular products with optimal potency, engraftment potential and persistence *in vivo*, recent studies have shown that minimally differentiated T cell phenotypes are preferred. However, genetic engineering of quiescent T cells remains challenging. Photoporation is an upcoming alternative non-viral transfection method which makes use of photothermal nanoparticles, such as polydopamine nanoparticles (PDNPs), to induce transient membrane permeabilization by distinct photothermal effects upon laser irradiation, allowing exogenous molecules to enter cells. In this study, we analyzed the capability of PDNP-photoporation to deliver large model macromolecules (FITC-dextran 500 kDa, FD500) in unstimulated and expanded human T cells. We compared different sizes of PDNPs (150, 250 and 400 nm), concentrations of PDNPs and laser fluences and found an optimal condition that generated high delivery yields of FD500 in both T cell phenotypes. A multiparametric analysis of cell proliferation, surface activation markers and cytokine production, revealed that unstimulated T cells photoporated with 150 nm and 250 nm PDNPs retained their propensity to become activated, whereas those photoporated with 400 nm PDNPs did less. Our findings show that PDNP-photoporation is a promising strategy for transfection of quiescent T cells, but that PDNPs should be small enough to avoid excessive cell damage.

1. Introduction

Intracellular delivery of plasma membrane-impermeable molecules, such as contrast agents or nucleic acids, is not only a common requirement for cell biological research, but also for the development of engineered cell-based therapies [1]. One of the most prominent examples of the latter is adoptive T cell transfer where T cells are genetically modified to express a chimeric antigen receptor (CAR) or T cell receptor (TCR) to increase their potency to recognize and kill tumor cells [2–4]. CAR T cell immunotherapy demonstrated durable clinical responses in relapsed and refractory B cell malignancies, leading to the regulatory approval of several CD19-specific CAR T cell therapies [5–9].

At present, 6 CAR T cell products are FDA approved for the treatment of hematological malignancies. To extend its possibilities towards the treatment of solid tumors, vast research efforts are aimed at improving CAR T cell potency and *in vivo* persistency. In this context, several preclinical and clinical studies demonstrated that intrinsic T cell properties, such as differentiation status, may be a critical determinant of patient response to treatment. Superior antitumor responses were observed for T cells with less differentiated phenotypes, such as naïve or central memory cells, correlating with robust *in vivo* expansion and persistence [10–16]. In contrast, prolonged *in vitro* culture drives cells towards terminal differentiation with increased expression of exhaustion markers and inhibitory receptors [10].

Generation of cellular products with optimal potency, engraftment potential and persistence can be achieved by shortening culture time, optimizing culture conditions (culture medium, cell density, cytokine supplementation, etc.), or modulation of metabolic pathways. Importantly, Ghassemi *et al.* previously showed that reducing the time of *ex vivo* culture to 3-5 days resulted in less differentiated CAR T cells with superior leukemia control at low cell doses when compared

to cells expanded for 9 days [17]. Recent reports even try to completely eliminate the activation and *ex vivo* expansion steps in order to maximize the therapeutic potential of CAR T cells [18,19]. For instance, Ghassemi and Milone demonstrated that functional CAR T cells can be generated from quiescent cells within 24 h of T cell collection by lentiviral transduction under optimized culture conditions. Importantly, these non-activated CAR T cells exhibited potent anti-leukemic *in vivo* activity at cell doses lower than those effective for activated CAR T cells produced using a standard 9-day protocol [18]. Nonetheless, genetic engineering of quiescent T cells remains challenging and is only reported in a very limited number of publications [20–22].

At present, the CAR T cell manufacturing process predominantly relies on retro- or lentiviral transduction to deliver the transgene into pre-activated T cells, followed by their *in vitro* expansion to achieve therapeutically required doses. Despite its satisfactory performance for the current generation of approved T cell therapies, viral vectors remain associated with several limitations [23–25]. GMP compliant viral vector production for clinical applications is a lengthy and costly process, requiring stringent quality control testing for the presence of replication-competent viruses in the final cell product. Furthermore, viral vectors carry an intrinsic risk of immunogenicity or insertional oncogenesis while offering limited cargo capacity, which may become problematic with the evolving CAR design. These challenges have spurred a growing interest in safer non-viral gene delivery technologies with a simpler and more cost-effective manufacturing process. This would result in greater availability and reduced vein-to-vein time for the benefit of patients, especially for those with rapidly progressing disease [26–28].

For genetic modification of T cells, techniques that physically induce membrane permeabilization have proven especially promising. These techniques use a physical stimulus to transiently permeabilize the cell membrane, allowing cargo molecules to enter the cytosol. Electroporation is

the best-known example, but it can induce high levels of acute toxicity and long-term adverse effects, diminishing the therapeutic potential of the final cell product [29–32]. In recent years, newer and gentler membrane permeabilization technologies have emerged which have much less impact on normal T cell functioning. Examples are cell squeezing [32], microneedles [31] and most recently, nanofiber-based photoporation [33].

In its traditional form, photoporation or optoporation is a physical delivery method based on laser irradiation of photothermal nanoparticles (NPs) that can attach to the cell membrane [34,35]. Depending on the applied laser energy, membrane permeabilization can be achieved by distinct photothermal effects (**Figure 1**). Application of a relatively low laser fluence results in direct heating of NPs that triggers local phase transitions in the lipid bilayer and glycoprotein denaturation [36]. When sufficiently high laser fluences are used, the NP temperature rises above the critical temperature of the surrounding liquid causing its almost instantaneous evaporation and formation of vapor nanobubbles (VNBs). Rapid expansion and collapse of VNBs lead to high-pressure waves and fluid shear stress that can generate transient pores in the plasma membrane [34,37,38]. The technology typically makes use of metallic nanoparticles, such as gold nanoparticles (AuNPs). AuNP-mediated photoporation has been successfully used to deliver various molecules such as siRNA, mRNA and Cas9 ribonucleoprotein (RNP) complexes in both murine and human T lymphocytes [39–41]. However, AuNPs in an aqueous environment are known to fragment under intense laser irradiation into smaller particles of a few nanometers. This represents a potential safety risk since very small AuNPs have been shown to intercalate with cellular DNA, potentially leading to genotoxic effects [42–46]. Moreover, the non-biodegradable nature of AuNPs presents safety and regulatory hurdles for the clinical translation of NP-mediated photoporation. To address these limitations, we have recently developed an alternative system

based on biocompatible and biodegradable polydopamine nanoparticles (PDNPs). PDNPs can be optically stimulated over the entire visible range, can be easily synthesized in a broad range of sizes, and their surface can be readily functionalized in a variety of ways [47]. Using PDNPs of about 0.5 µm in size as photoporation sensitizers we could successfully transfect activated and expanded human T cells with mRNA [48].

It remains unknown whether PDNP photoporation is equally suited to deliver macromolecules in quiescent T cells and to what extent it impacts their fitness and functionality. Therefore, we have here compared macromolecule delivery by PDNP-photoporation in unstimulated and expanded T cells. Since unstimulated T cells are substantially smaller than activated T cells, we decided to test smaller sizes of PDNPs than before. PDNPs of three different nominal sizes were first synthesized (150 nm, 250 nm and 400 nm), after which the PDNP concentration and laser fluence was determined which leads to the best intracellular delivery yield of FITC-dextran 500 kDa as a model macromolecule. For the optimized conditions, we investigated cell functionality by testing the propensity of quiescent cells to become activated after PDNP-photoporation. T cell activation was determined by analyzing cell proliferation, expression of surface activation markers and secretion of effector cytokines.

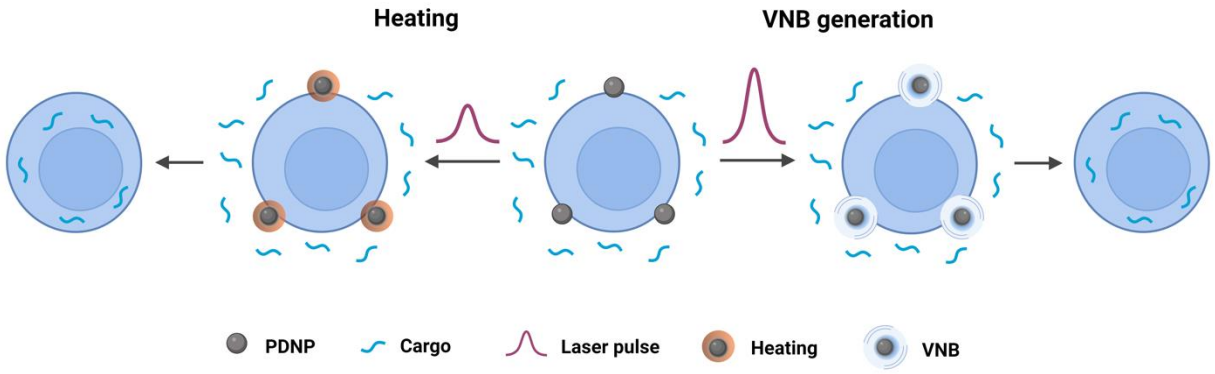

Figure 1. Overview of PDNP photoporation procedure for intracellular delivery of macromolecules in T cells. First, BSA-coated polydopamine nanoparticles (PDNPs) and macromolecules of interest are added to the cells. Depending on the applied laser energy, transient cell membrane permeabilization can be achieved either by photothermal heating or the generation of vapor nanobubbles (VNBs), allowing the exogenous cargo to diffuse into the cell cytoplasm. Created with BioRender.com

2. Materials and methods

2.1. Human T cell isolation and culture

Healthy donor buffy coats were obtained from the Red Cross Flanders Biobank (Ghent, Belgium) and used following the guidelines of the Medical Ethical Committee of Ghent University Hospital (Ghent, Belgium). Peripheral blood mononuclear cells (PBMCs) were isolated via density gradient centrifugation with Lymphoprep (Stem Cell Technologies, Vancouver, Canada). Next, human pan CD3+ T cells were isolated by a magnetic negative selection using the EasySep Human T cell enrichment Kit (Stem Cell Technologies, Vancouver, Canada) according to the manufacturer's protocol. Unstimulated cells were maintained in Iscove's modified Dulbecco's medium (IMDM) GlutaMAX (Gibco, Merelbeke, Belgium), supplemented with 10% heat-inactivated fetal bovine serum (FBS, Biowest), 100 U/mL penicillin and 100 µg/mL streptomycin (P/S, Gibco, Merelbeke, Belgium) and treated by photoporation on the day of isolation. Alternatively, T cells were stimulated with ImmunoCult Human CD3/CD28 T cell Activator (Stem Cell Technologies, Vancouver, Canada) according to the manufacturer's instructions. Activated cells were supplemented with 10 ng/mL IL-2 (PeproTech, United Kingdom) and kept in culture for 7 days before the photoporation treatment.

2.2. Visualization of unstimulated and expanded T cells by confocal microscopy

Unstimulated and expanded T cells were stained with Hoechst 33342 (Invitrogen, Belgium) and CellMask Deep Red Plasma membrane stain (Invitrogen, Belgium). Samples were visualized with a Nikon A1R HD confocal laser scanning microscope (Nikon Benelux, Belgium) with a 60x water immersion lens (SR plan apo IR 60X WI, NA 1.3, WD 180µm). 408 nm and 633 nm laser lines were used for Hoechst and Cy5/Deep red (Cell Mask), respectively. Fluorescence was detected through a 450/50 nm (MHE57010) and 700/75nm (MHE57070) emission filter on a Multi-Alkali PMT (A1-DUG-2 GaAsP Multi Detector Unit, Nikon), respectively. A galvano scanner was used for unidirectional scanning to acquire the channels sequentially at a scan speed of 0.5 FPS with 2X line averaging. The pinhole was set to 1.2 AU. The pixel size was set to 90 nm/pixel. ImageJ (FIJI) software [49] was used to process the images and average T cell sizes were determined by manual measurement of cell diameter (minimum 100 cells per cell phenotype).

2.3. Synthesis and physicochemical characterization of polydopamine nanoparticles

The synthesis of polydopamine nanoparticles (PDNPs) was based on a protocol originally reported by Ju *et al.* [50], and later adapted by Harizaj *et al.* [48]. Briefly, dopamine hydrochloride powder (Sigma-Aldrich) was dissolved in HyClone water (HyPure, Cell Culture Grade, VWR) at a concentration of 3.5 mg/mL at 50°C. Next, 1M NaOH solution was added under vigorous stirring at a fixed molar ratio of 1:0.8, turning the solution pale yellow first, and eventually dark brown. The solution was left to stir for approximately 7 h and the hydrodynamic diameter of the particles was monitored every hour by dynamic light scattering (DLS, Zetasizer Nano ZS, Malvern Instruments Co., Ltd). To reduce potential particle aggregation, the suspensions were sonicated at 10% amplitude for 30 seconds with a tip sonicator (Branson Digital Sonifier, Danbury, USA).

Once the desired hydrodynamic diameter was achieved, nanoparticles were retrieved by centrifugation and were washed several times with HyClone water. For 150 nm PDNPs, the NP suspension was transferred to 1.5 mL Eppendorf tubes and PDNPs were washed with HyClone water by centrifugation (21.000 rcf, 20 minutes). For 250 nm PDNPs, the suspension was collected in 50 mL conical tubes and the PD NPs were washed with HyClone water by centrifugation (4.000 rcf, 20 minutes). 400 nm PDNPs were also collected in 50 mL conical tubes and were washed with HyClone water by centrifugation (4.000 rcf, 10 minutes).

Next, to increase the colloidal stability of PDNPs in suspension and improve their interaction with cell membranes, a functionalization with bovine serum albumin (BSA, Biotechnology grade, VWR Chemicals, USA) was performed. The uncoated PDNP suspension was mixed with a 10 mg/mL BSA solution in DPBS at a 1:1 volume ratio. The mixture was then allowed to react by vigorous stirring overnight and the remaining unbound BSA was removed by several washing steps with HyClone water. The following centrifugation speeds were used for different sizes: 150 nm PDNPs (21.000 rcf, 20 minutes), 250 nm PDNPs (4000 rcf, 20 minutes) and 400 nm PDNPs (4000 rcf, 10 minutes). The resulting BSA-coated PD NPs were dispersed in HyClone water and stored at 4°C.

To provide additional evidence for successful BSA coating, 400 nm PDNPs were coated with albumin−fluorescein isothiocyanate conjugate (FITC-BSA, Sigma-Aldrich) as described for the coating with standard BSA. PDNP dilutions (at $5.6x10^8$ NPs/mL) were added to wells of a glass-bottom 96-well plate and left to dry overnight at 37ºC. Next, ProLong™ Diamond antifade mountant (Invitrogen, Belgium) was added and samples were allowed to cure for 24 h at room temperature. Samples were visualized with a Nikon A1R HD confocal laser scanning microscope (Nikon Benelux, Belgium) with a 60x oil immersion lens (plan apo λ 60X oil, NA 1.4, WD 130

μm). The PDNP core particles were visualized in light scattering mode using a 80/20 beam splitter, while the FITC-BSA coating was visualized in the green fluorescent channel using a 525/50nm emission filter (MHE57030, Nikon). A galvano scanner was used for unidirectional scanning to acquire the channels sequentially. Scan speed was set to 0.125 FPS with 16X line averaging. The pinhole was set to 1.2 AU. The pixel size was set to 110 nm/pixel. ImageJ (FIJI) was used to process the images.

Additionally, relative florescence intensities of uncoated and FITC-BSA-coated PDNP dilutions were measured using a VICTOR3 1420 Multilabel Counter® (Perkin Elmer) with excitation at 485 nm and emission at 535 nm.

To visualize the particles by scanning electron microscopy (SEM), BSA-coated PDNPs were dried on silicon wafers one day before the measurement. SEM images were acquired with a FEI Quanta 200F microscope (Thermo Fisher) operating at a voltage of 20 kV. Dynamic light scattering (DLS, Zetasizer Nano ZS, Malvern Instruments Co., Ltd.) was used to measure the hydrodynamic diameter and nanoparticle tracking analysis (NTA, NanoSight LM10, Malvern Panalytical, UK) was performed to determine nanoparticle concentrations [51–53]. NTA was performed in scattering mode with a 488 nm laser.

To estimate the mass concentration of PDNPs administered to cells, a spherical shape of nanoparticles was assumed with a PDNP density of 1.52 g/cm^3 as previously reported in the literature [54]. For spherical nanoparticles, the volume is $V=4/3\pi r^3$, where r is the radius of the sphere (based on NP diameters measured from SEM images). Next, the mass of single NP was calculated by multiplying NP volume by polydopamine density, from which the mass

concentrations are finally obtained. The conversion between PDNP number [NPs/mL] and mass [mg/mL] concentrations is reported in Table S3 in Supporting Information.

2.4. Determination of VNB generation threshold

For the generation and detection of VNBs, an in-house developed setup equipped with a 3 ns pulsed 532 nm laser (Cobolt Tor^{TM} Series, Cobolt AB, Solna, Sweden) was used to illuminate the PDNPs. The stocks of PDNPs were first diluted in ddH_2O to a concentration of ~ $1x10^9$ NPs/mL, next samples were transferred to 50 mm γ-irradiated glass bottom dishes (MatTek Corporation, Ashland, MA, USA) and particles were allowed to sediment on the bottom. Lasers pulses were generated using a 25 MHz pulse generator (TGP3121, Aim-TTi, Huntingdon, UK), with control over the pulse energy being provided by an adjustable DC power supply (HQ Power PS23023, Velleman Group, Gavere, Belgium). The VNBs were visualized using dark field microscopy, where the increased scatter of VNBs resulted in bright white spots on a black background. The number of VNBs visible within the irradiated region was quantified for increasing laser pulse fluences. These VNB numbers were then plotted in the function of laser pulse fluence and a Boltzmann sigmoid curve was fitted to determine the threshold, defined as the laser fluence at which there is a 90% probability of a given particle generating a VNB.

2.5. Photoporation for the delivery of FITC-dextran 500 kDa

FITC-dextran of 500 kDa (FD500, Sigma-Aldrich, Bornem, Belgium) was used as a model macromolecule for measuring delivery efficiency and optimizing photoporation parameters. FD500 delivery was performed in either unstimulated or activated and expanded human T cells. Opti-MEM was selected as the transfection buffer of choice. The cells were first washed three

times by centrifugation (300xg, 5 min) with Opti-MEM to remove any residual cell culture medium with FBS. After the final washing step, cells were resuspended in Opti-MEM and transferred to a flat-bottom 96-well plate ($1x10^6$ cells per well). Next, a series of PDNP dilutions was prepared in Opti-MEM and added to cell suspensions to reach concentrations specified in the results. Finally, FD500 was added to the mixture to reach a final concentration of 1 mg/mL.

The plate was quickly spun down to let the cells sediment to the bottom of the plate. Photoporation was then performed with an in-house developed setup with a nanosecond laser (3 ns pulse duration, 532 nm wavelength) and equipped with a galvano scanner, enabling irradiation in high throughput (3-4 s per well). Immediately after laser treatment, cells were washed three times by centrifugation (300xg, 5 min), resuspended in fresh culture medium, and incubated at 37°C, 5% CO_2 until the moment of analysis of delivery efficiency and cell viability.

To evaluate the delivery efficiency of FD500 (i.e., the percentage of FITC-positive cells), T cells were washed once with DPBS- (300xg, 5 min) and resuspended in flow buffer (DPBS-, 1% BSA, 0.1% Sodium Azide) with TO-PRO3 iodide (Invitrogen, Belgium) as cell viability dye. Flow cytometry was performed using a MACSQuant Analyzer 16 (Miltenyi Biotec, Germany) and a minimum of 40 000 cells were analyzed per sample. FITC and TO-PRO-3/ APC were excited with 488 and 640 nm lasers and detected with 525/50 and 655-730 nm filters, respectively. FlowJo™ software (Treestar Inc.) was used for data analysis.

2.6. T cell activation after photoporation of unstimulated T cells

To determine to which extent quiescent T cells can still be stimulated after being treated with photoporation, unstimulated T cells were treated by photoporation as described before but in the absence of cargo molecules. This allows assessing the influence of the photoporation treatment

alone, excluding potential confounding effects due to the intracellularly delivered cargo molecules. After laser treatment, the cells were rested overnight at 37°C, 5% CO_2. The next day, cells were stimulated with ImmunoCult Human CD3/CD28 T cell Activator (Stem Cell Technologies, Vancouver, Canada) according to the manufacturer's protocol. Briefly, T cells ($1x10^6$/mL) were seeded in 24-well plates in complete IMDM supplemented with 10 ng/mL IL-2 and 25 uL of CD3/CD28 Activator was added per well. Cultures were split and supplemented with fresh medium on day 3, day 5 and day 7.

As a control, T cells were mixed with PDNPs but without applying laser irradiation. After exposure to PDNPs, cells were activated as described above.

For the analysis of surface activation markers by flow cytometry, the following anti-human monoclonal antibodies were used: CD3 FITC (StemCell Technologies, Vancouver, Canada), CD3 PE/Cy7 (Biolegend, USA), CD154 FITC (Biolegend, USA), CD137 PE (Biolegend, USA), HLA-DR PerCP (Biolegend, USA), PD-1 APC (Biolegend, USA) and PD-1 PE (Miltenyi Biotec, Germany). Briefly, cells were washed with DPBS, resuspended in flow buffer and incubated with the indicated antibodies for 30 min at 4°C. LIVE/DEAD™ Fixable Aqua Stain (Invitrogen, Belgium) or TO-PRO™-3 iodide (Invitrogen, Belgium) were included in the staining panels to distinguish between live and dead cell populations. After two washing steps, samples were measured on a MACSQuant Analyzer 16 (Miltenyi Biotec, Germany). LIVE/DEAD™ Aqua Stain and TO-PRO-3/ APC were excited with 405 and 640 nm lasers and detected with 525/50 and 655-730 nm filters, respectively. FITC, PE, PerCP and PE-Cy7 were excited with a 488 nm laser and collected with the respective filters of 525/50 nm, 585/40 nm, 655-730 nm, and 750 nm LP. FlowJo software (Treestar Inc.) was used for data analysis.

2.7. Evaluation of cell viability with Cell Titer Glo assay

The CellTiter Glo® luminescent cell viability assay (Promega, Belgium) was used according to the manufacturer's instructions to assess cell viability after photoporation or to monitor T cells stimulated after pre-treatment by photoporation. In this assay, the number of viable cells is determined by quantitation of the ATP present, as an indicator of metabolically active cells. Briefly, T cells in complete culture medium were supplemented with an equal volume of CellTiter Glo® reagent and shaken on an orbital shaker (120 rpm) for 10 min at room temperature. Next, the cell lysates were transferred to an opaque 96-well plate and the luminescent signal was measured using a GloMax® microplate reader (Promega, Belgium) with a detection wavelength range of 350 to 650 nm. Cell viability was calculated relative to the non-treated control.

The cell viability readout was then combined with delivery efficiency measured by flow cytometry to obtain the delivery yield, a parameter representing the viable and successfully transfected fraction compared to the initial cell population. The delivery yield percentage can be calculated by multiplying the percentage of FD500-positive cells and the percentage of viable cells:

Delivery yield [%] = (delivery efficiency [%] x cell viability [%]) /100

2.8. Cell counting with Trypan Blue

To monitor cell viability and proliferation of T cells activated after photoporation treatment, cells were counted manually using a Bürker counting chamber (Brand GMBH, Germany) and trypan blue exclusion staining (0.4%, Sigma-Aldrich, Belgium). Cell number changes were normalized to the starting seeding density of $1x10^6$ cells/mL on day 1 and corrected for culture dilutions at the previously indicated time points.

2.9. Quantification of cytokines in cell culture supernatants

Cell culture supernatants were collected at the indicated time points and stored at -80°C. The production of interferon gamma and Tumor Necrosis Factor alpha was determined using the Human IFN gamma ELISA kit (Invitrogen, Belgium) and the Human TNF alpha ELISA kit (Invitrogen, Belgium), according to the manufacturer's protocols. The absorbance was measured at 450 nm with a VICTOR3 1420 Multilabel Counter® (Perkin Elmer). The results are presented both without normalization and normalized to cell numbers.

2.10. Statistical analysis

All data are shown as mean ± standard deviation (SD). Statistical differences were analyzed using GraphPad Prism 8 software (La Jolla, USA). Two-way ANOVA with Tukey's multiple comparisons test was used to compare maximal FD500 delivery yields achieved with different PDNP sizes and laser fluences, and to analyze cell proliferation rates in cultures pre-treated by photoporation. Expression of surface activation markers and cytokine production were evaluated using Kruskal-Wallis nonparametric test with Dunn's multiple comparisons test. Asterisks are used to illustrate statistical significance (* $p < 0.05$; ** $p < 0.01$; *** $p < 0.001$; **** $p < 0.0001$).

3. Results

3.1. Characterization of unstimulated and activated T cells by confocal microscopy

In this study, we aimed to investigate the applicability of PDNP-photoporation for the intracellular delivery in unstimulated and expanded T cells. As it is well known that activated T cells are larger than quiescent T cells [55,56], we reasoned that it would be of interest to evaluate different sizes of PDNPs. To better understand the morphological differences between these two cell phenotypes and guide the selection of photothermal NP sizes, we first visualized unstimulated and pre-activated T cells by confocal microscopy after nuclear and cell membrane staining (**Figure 2**). The average cell diameters quantified from confocal images were 7 ± 0.5 µm for the unstimulated (**Figure 2C**) and 12.6 ± 2 µm for the activated T cells (**Figure 2D**).

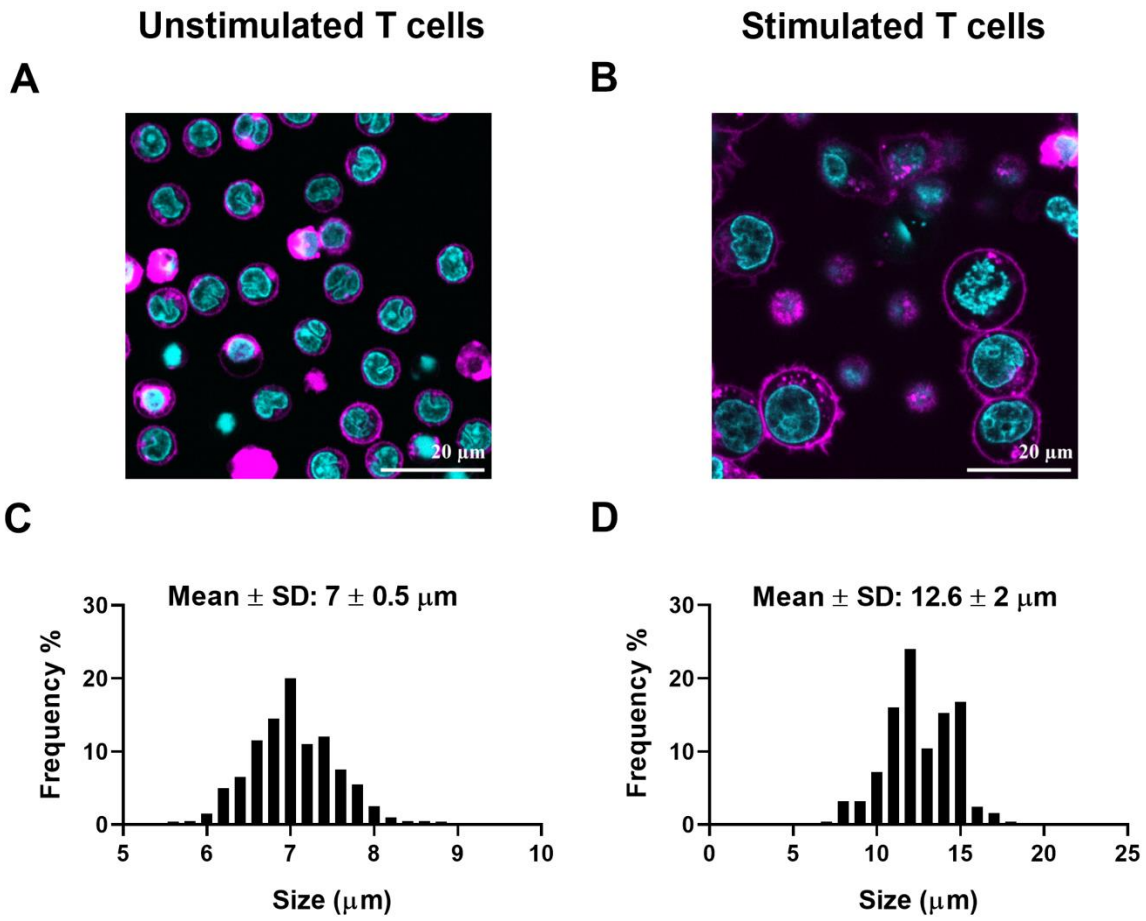

Figure 2. Visualization of unstimulated and activated T cells by confocal microscopy. (A, B) Representative confocal images of unstimulated (A) and activated (B) T cells. T cell nuclei and cell membranes were stained with Hoechst 33342 (cyan) and CellMask Deep Red stain (magenta), respectively. The scale bar represents 20 µm. (C, D) Size distribution of unstimulated (C) and activated (D) T cells, as derived from the confocal images.

3.2. Synthesis and physicochemical characterization of polydopamine nanoparticles

The synthesis of polydopamine nanoparticles (PDNPs) was performed according to the protocol adapted by Harizaj *et al.* [48] and is based on the neutralization of dopamine hydrochloride with NaOH, followed by spontaneous air oxidation (cfr. M&M) [50]. The size of particles is affected by various synthesis parameters, such as reaction temperature, pH and dopamine concentration

[50,57]. Using a dopamine hydrochloride/NaOH ratio of 1:0.8 and a reaction temperature of 50°C, a gradual growth of PDNPs was achieved. Size was monitored at regular time intervals by dynamic light scattering (DLS). Sonication was applied to remove any remaining agglomerates as previously reported by Harizaj *et al.* [48]. Once the desired size was reached, the reaction was terminated and the PDNPs were retrieved by centrifugation.

The uncoated PDNPs displayed excellent colloidal stability in water but tended to aggregate in Opti-MEM (**Figure S1** and **Table S1**, Supporting Information), calling for an extra functionalization step to ensure good stability in transfection media that are typically used in cell experiments. Serum albumins have been widely used in biomedical applications such as the synthesis of multifunctional nanoparticles for drug delivery and bioimaging or ultrathin coatings of nanostructures to enhance their immune compatibility [58–60]. In the present study we opted for PDNP functionalization with bovine serum albumin (BSA), which is based on a Schiff base type or Michael addition reaction between amine groups of albumin and catechol/ quinine groups of polydopamine and can be achieved by overnight incubation of PDNPs with BSA solution [61–63]. After PDNP functionalization, an increase in hydrodynamic diameter from 493 ± 3 nm to 522 ± 3 nm was observed (**Table S1**, Supporting Information), providing a first indication of successful coating. This observation was in agreement with other studies reporting BSA coatings with a thickness in the nanometer scale [60,64,65]. In addition, the zeta-potential turned slightly negative after the coating procedure (**Table S2**, Supporting Information), similar to what was previously reported by Harizaj *et al*. [48]. To provide further evidence for effective BSA coating, PDNPs were functionalized with FITC-conjugated BSA and visualized by confocal microscopy (**Figure S2**, Supporting Information). The PDNP core particles were visualized by in light scattering mode, while the FITC-BSA coating was visualized in the green fluorescent channel. We were able to

successfully detect fluorescence for FITC-BSA-coated particles, which was not the case for the uncoated PDNPs. These results were finally complemented with a spectrometric analysis of relative fluorescence intensities of FITC-BSA-coated and uncoated PDNPs (**Figure S3**, Supporting Information). Together these data show that a BSA coating could be successfully applied to the PDNPs.

BSA-coated PDNPs of three different dimensions were created, of which the size and morphology was analyzed by SEM (**Figure 3A**, **3B**, **3C**). Each formulation showed a near-spherical shape of fairly uniform size. Using image analysis, we measured respective PDNP diameters of 141 ± 18 nm (**Figure 3D**), 238 ± 34 nm (**Figure 3E**) and 385 ± 42 nm (**Figure 3F**). For ease of reference, we will refer to those particles as 150 nm, 250 nm and 400 nm PDNPs, respectively. The hydrodynamic diameter of the PDNPs was additionally assessed by DLS in water and Opti-MEM, of which representative intensity size distributions are displayed in **Figure 3G**, **3H** and **3I**. The average hydrodynamic size was respectively 145 ± 1 nm, 237 ± 5 nm and 471 ± 1 nm in water, and 149 ± 1 nm, 255 ± 4 nm and 460 ± 6 nm in Opti-MEM (**Table S2,** Supporting Information). All formulations were characterized by quite low polydispersity index (PDI) values in both water and Opti-MEM, indicating relatively narrow size distributions [66,67]. This shows that PDNPs are stable in Opti-MEM which is used to add them to cells. In addition, the BSA-PDNP size was determined after mixing with FD500, which is a model cargo molecule used in the present study. As can be seen in **Figure S4**, no change in size was observed, showing that BSA-PDNPs do not aggregate in the presence of FD500.

While the hydrodynamic size measured by DLS corresponded well with the particle diameters measured with SEM, 400 nm PDNPs appeared larger when measured with DLS. This may be due

to the presence of spurious aggregates (dimers or small agglomerates) that cannot be discriminated from individual particles with DLS. Nevertheless, overall, there was a good correspondence between SEM and DLS size measurements. Next, we investigated whether differently sized PDNPs can generate VNBs when irradiated with pulsed laser light (**Figure 3J**, **3K**, **3L**). VNBs can be visualized by dark field microscopy as they intensely scatter light during their lifetime. By counting the number of VNBs as a function of the applied laser fluence and by fitting the plotted data with a Boltzmann function, the VNB threshold can be determined, which is defined as the laser fluence at which 90% of the NPs present in the irradiated region generate VNBs. For 400 nm PDNPs, the threshold laser fluence was determined to be 1.32 J/cm^2. 250 nm PDNPs generated bubbles when illuminated with higher laser fluences, however, no saturation of the VNB formation could be reached within the range of fluences available on our optical setup, hence no threshold could be determined. Lastly, for 150 nm PDNPs, no VNBs were detected, even at the highest available laser fluence. These results are in agreement with the observations of Harizaj *et al.*, who previously reported an increasing VNB threshold for decreasing PDNP sizes.

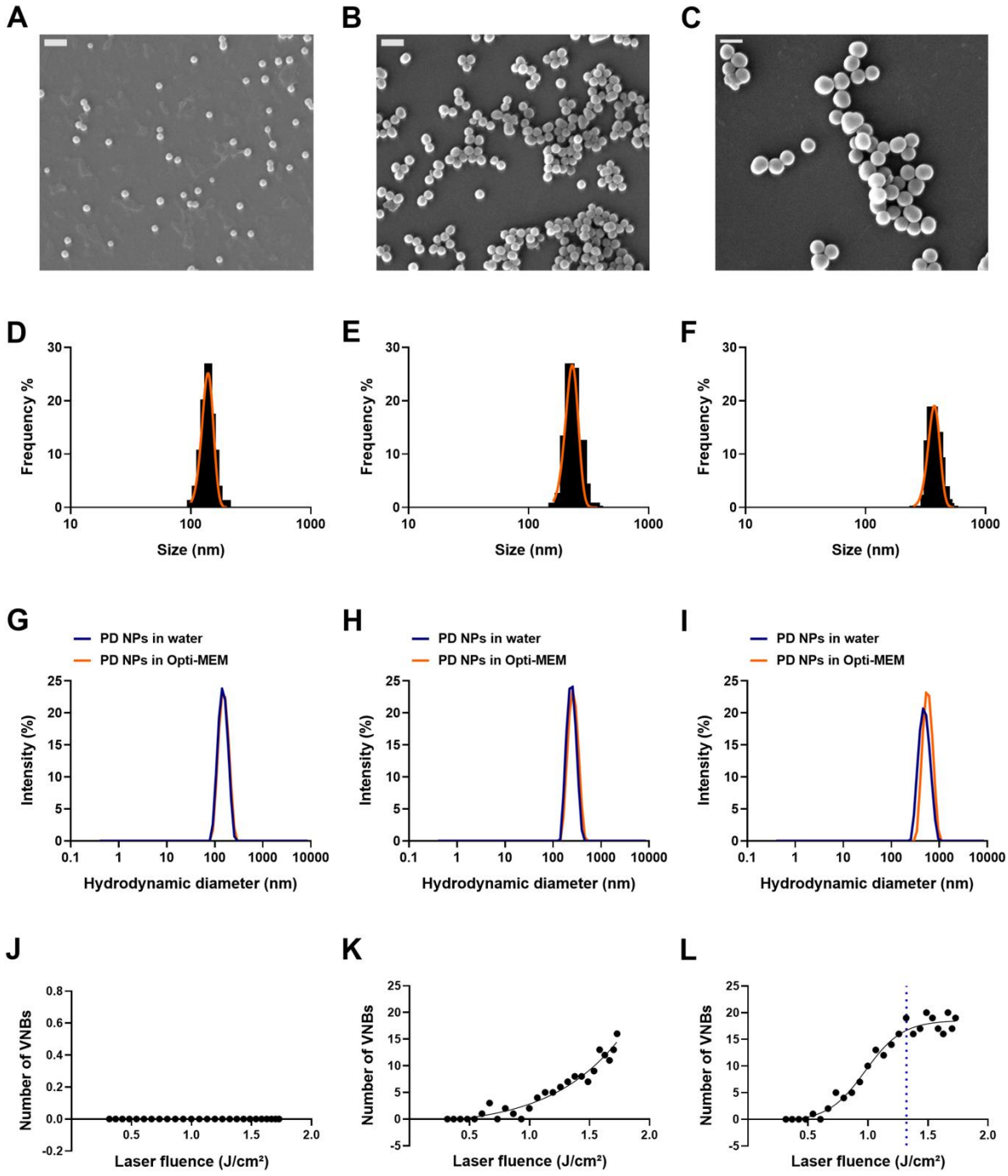

411

412

413 **Figure 3. Physicochemical characterization of BSA-coated polydopamine nanoparticles (PDNPs) of different**
414 **sizes.** (A-C) Representative SEM images of 150 nm (A), 250 nm (B), and 400 nm (C) PDNPs. The scale bar
415 corresponds to 500 nm. (D-F) Size distribution of 150 nm (D), 250 nm (E), and 400 nm (F) PDNPs, as derived from

the SEM images. (G-I) Representative intensity size distributions of BSA-coated PDNPs of 150 nm (G), 250 nm (H), and 400 nm (I) as measured by DLS in water (blue curve) and Opti-MEM (orange curve). (J-L) Determination of vapor nanobubble (VNB) generation threshold for 150 nm (J), 250 nm (K) and 400 nm (L) PDNPs. The number of bubbles was determined for increasing laser pulse fluences using dark field microscopy. The VNB threshold is deduced using a Boltzmann fit (solid line) and is defined as the laser pulse fluence at which 90% of the asymptotic value of the Boltzmann fit is obtained (blue dotted line).

3.3. Intracellular delivery of FD500 in unstimulated T cells

To evaluate the efficiency of intracellular delivery by PDNP photoporation in unstimulated human T cells, FD500 was selected as a model compound. The procedure of isolating unstimulated T cells from blood samples and application of the photoporation procedure is schematically depicted in **Figure 4A**. For each particle size, T cells were incubated with a range of PDNP concentrations and irradiated with three different laser fluences, *i.e.*, 0.56 J/cm^2, 1.06 J/cm^2 and 1.45 J/cm^2, the latter being close to the highest fluence that can be reached on the photoporation setup used in this study. The percentage of FD500+ cells (readout for delivery efficiency), as quantified by flow cytometry, gradually increased with PDNP concentration, gradually approaching near 100% positive cells (**Figure 4B, 4C, 4D**). The increase in delivery efficiency was associated with decreasing cell viability, which was assessed two hours after photoporation using a Cell Titer Glo assay. The delivery yield, the percentage of FD500+ cells which are alive, was unique to PDNP size (**Figure 4E**, **4F**, **4G**). For 150 nm PDNPs the most optimal PDNP concentration was consistently 256×10^{10} NPs/mL, while it was 8×10^{10} NPs/mL for 250 nm PDNPs and 2×10^{10} NPs/mL for 400 nm PDNPs. The delivery efficiency for those concentrations was higher for higher laser fluences, but due to a proportionally higher cytotoxicity, the optimal yield values were not significantly different for different laser fluences. Finally, the delivery yield increased with decreasing PDNP size, with the yields being statistically different for treatment with 150 nm

PDNPs compared to 400 nm PDNPs ($p < 0.001$ for treatment with 1.06 J/cm^2; $p < 0.01$ for 0.56 J/cm^2 and 1.45 J/cm^2).

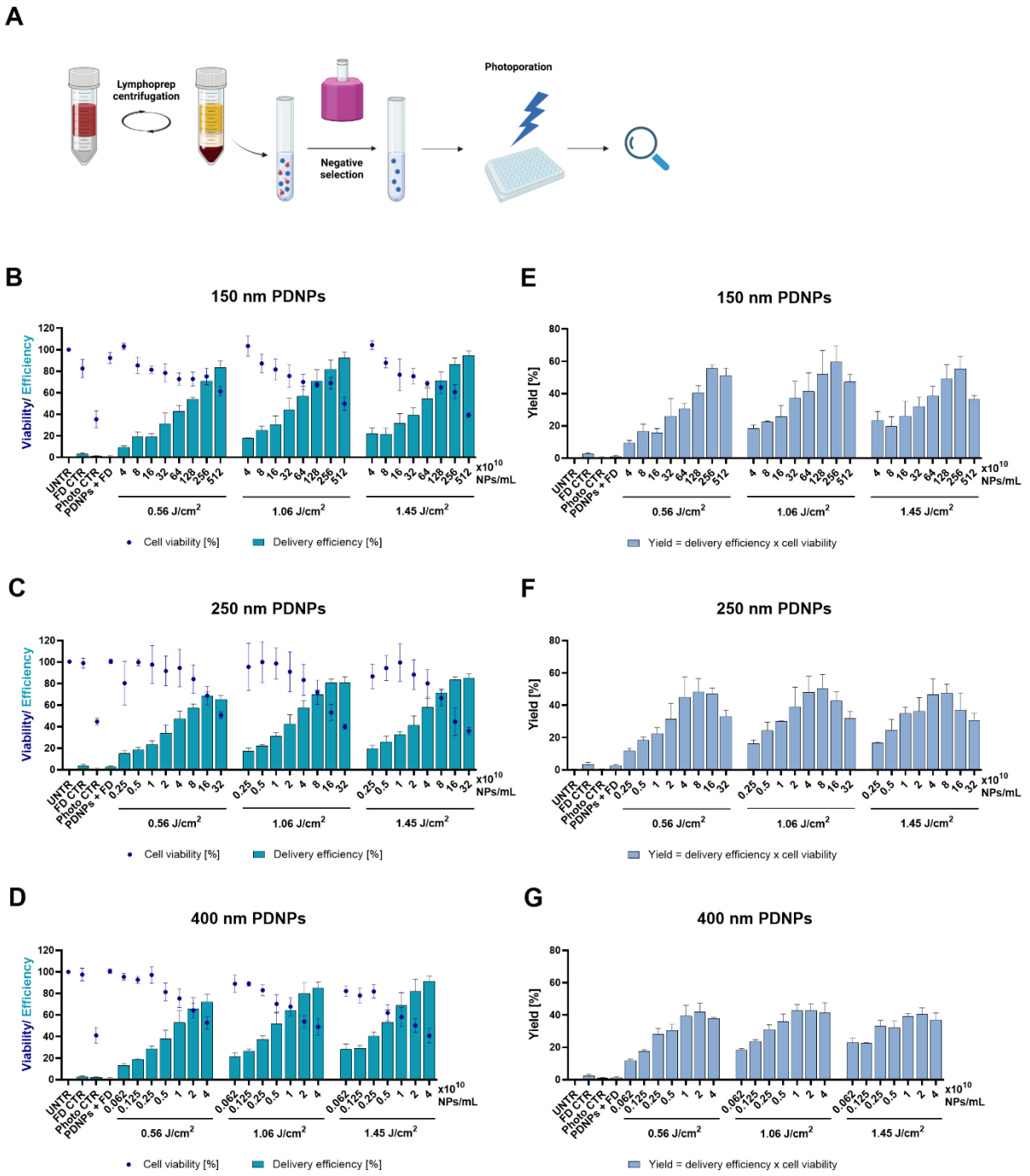

Figure 4. Intracellular delivery of FD500 in unstimulated human T cells by PDNP photoporation. (A) Schematic overview of the experimental procedure (created with BioRender.com). Unstimulated T cells were treated by photoporation for the intracellular delivery of FD500 on the day of isolation. T cells were mixed with increasing concentrations of PDNPs of different sizes and irradiated with three laser fluences of 0.56, 1.06 and 1.45 J/cm^2. Untreated cells (UNTR), cells incubated with FD500 (FD CTR), cells incubated with FD500 and PDNPs (PDNPs + FD) and cells mixed with NPs and irradiated in the absence of cargo (photo CTR) served as control conditions. (B-D) Delivery efficiency of FD500 (bars) was measured by flow cytometry and cell viability (dots) was determined by a Cell Titer Glo assay 2 hours after the treatment. (E-G) Delivery yield represents the viable and transfected fraction of the initial cell population and was calculated as the product of delivery efficiency and cell viability. Data represent the mean ± SD of at least four different donors tested per PDNP size.

3.4. Intracellular delivery of FD500 in expanded T cells

Next, we performed the same experiment on expanded T cells. In this case, as schematically shown in **Figure 5A**, lymphocytes were activated with anti-CD3 and anti-CD28 antibodies and cultured in the presence of IL-2 for 7 days before being treated by photoporation in exactly the same manner as before. Again, higher percentages of FD500+ cells (delivery efficiency) could be observed with increasing PDNP concentration, at the expense of cell viability (**Figure 5B**, **5C**, **5D**). Again, higher laser fluence led to higher delivery efficiency, but due to higher toxicity there was no appreciable difference in the optimal delivery yield. For 150 nm PDNPs, the optimal PDNP concentration was 128-256×10^{10} NPs/mL, similar as for unstimulated T cells. For 250 nm PDNPs the optimal concentration was 8-16×10^{10} NPs/mL, again close to what was found for unstimulated T cells. For 400 nm PDNPs the optimal concentration varied between 0.25 and 1×10^{10} NPs/mL due to a relatively high variability between donors. This is slightly lower than for unstimulated T cells. But, considering high variability between donors, we conclude that the optimal PDNP concentration is very similar for unstimulated or expanded T cells. When looking at the effect of particle size,

PDNPs of 250 nm produced the highest yield, although the difference with other sizes was not statistically significant. Therefore, PDNP size had less influence on photoporation efficiency of expanded T cells. While the exact reason for this remains elusive, it may be related to the fact that unstimulated T cells are smaller than activated T cells (**Figure 2**) and, therefore, may be more sensitive to the size of PDNP (and of the induced membrane pores).

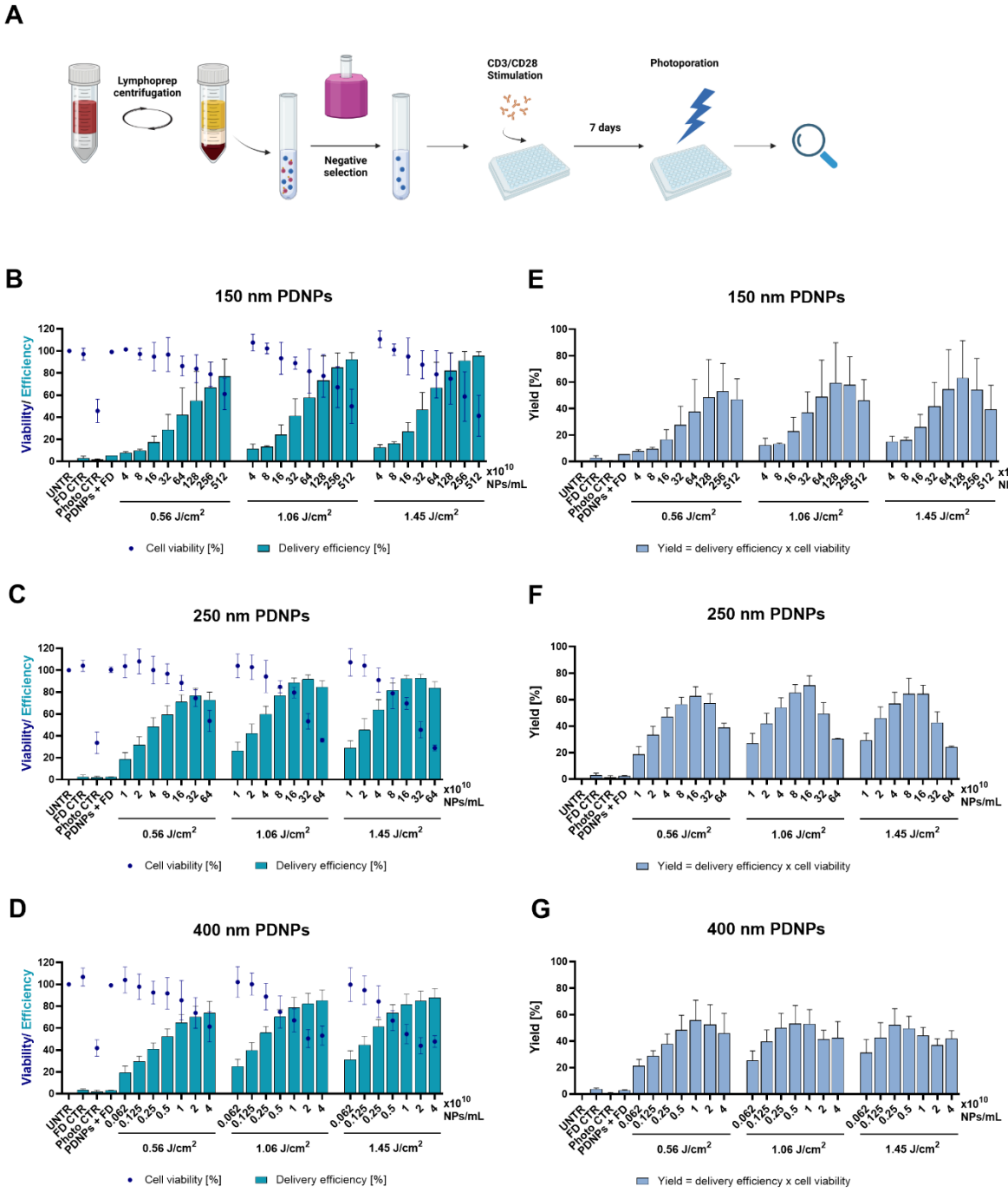

Figure 5. Intracellular delivery of FD500 in expanded human T cells by PDNP photoporation. (A) Schematic overview of the experimental procedure (created with BioRender.com). T cells were stimulated with ImmunoCult CD3/CD28 Activator and cultured for 7 days before photoporation treatment. Cells were mixed with increasing concentrations of PDNPs of different sizes and irradiated with three laser fluences of 0.56, 1.06 and 1.45 J/cm^2.

Untreated cells (UNTR), cells incubated with FD500 (FD CTR), cells incubated with FD500 and PDNPs (PDNPs + FD) and cells mixed with NPs and irradiated in the absence of cargo (photo CTR) served as control conditions. (B-D) Delivery efficiency of FD500 (bars) was measured by flow cytometry and cell viability (dots) was determined by a Cell Titer Glo assay 2 hours after the treatment. (E-G) Delivery yield represents the viable and transfected fraction of the initial cell population and was calculated as the product of delivery efficiency and cell viability. Data represent the mean ± SD of at least four different donors tested per PDNP size.

3.5. Evaluation of T cell functionality after pre-treatment by photoporation

Delivery efficiency and cell viability are the two most common success metrics in the assessment of intracellular delivery methods. However, for cell-based therapies, it is of critical importance to understand the impact of the applied transfection method on cell phenotype and function after treatment. T cell activation is one of the central events in the adaptive immune response, necessary for the generation of cellular and humoral immunity. Having optimized the photoporation parameters, we sought to investigate the functionality of cells irradiated with differently sized PDNPs by assessing their activation propensity after laser exposure. To this end, we measured cell proliferation, upregulation of activation markers and cytokine production (**Figure 6A and Figure S5)**. Unstimulated T cells were first exposed to photoporation in the absence of cargo using optimized PDNP concentrations, *i.e.*, $256x10^{10}$ NPs/mL (150 nm PDNPs), or $8x10^{10}$ NPs/mL (250 nm PDNPs), or $2x10^{10}$ NPs/mL (400 nm PDNPs), hereafter referred to as *photo 150*, *photo 250* and *photo 400*, respectively. Laser irradiation was performed at an intermediate laser fluence of 1.06 J/cm² and cells were then rested overnight. Before stimulation with CD3/CD28 tetrameric antibody complexes and IL-2, the cell density was adjusted to $1x10^6$ cells/mL in each experimental group to compensate for cell loss. Unstimulated cells cultured in a plain medium without activating agents were additionally included as a control condition (**Figure S5**). To evaluate T cell expansion,

we measured cell proliferation for up to 10 days by manual cell counting and a spectrophotometric metabolic (ATP quantification) assay. Based on cell counting, a statistically significant ($p < 0.05$) decreased proliferation potential was only observed at day 10 for photo 400-treated cells when compared to the untreated culture, whereas there were no statistically significant differences for the other conditions (**Figure 6B**). The ATP levels of photo 150-treated T cells remained comparable to the untreated ones throughout the whole culture period (**Figure 6C**). However, for photo 250-treated T cells, a significant decrease in viable cell numbers was noticed from day 5 on, stabilizing at 55 ± 24% at day 10. Photo 400-treated T cells turned out to be more heavily affected, with ATP rates being significantly lower than in the untreated culture and other conditions ($p < 0.001$), dropping to ~20-30% at the end of culture.

Next, we evaluated the expression of well-established surface activation markers, including CD154 (CD40L), CD137 (4-1BB), HLA-DR and activation/exhaustion marker PD-1 (**Figure 6D**). Since these antigens are known to display different kinetics of expression upon T cell stimulation [68–70], they were analyzed at two different time points: day 3 and day 5. Significantly diminished expression of CD154 and HLA-DR was observed at day 3 for photo 400-treated cells but not for photo 150- or photo 250-treated cells. No significant differences in expression profiles of CD137 and PD-1 were found.

Finally, the production of key effector cytokines such as IFNγ and TNFα was analyzed (**Figure S6 and 6E**). In line with proliferation readouts, a heavily diminished secretion of IFNγ was observed at day 3 and 5 for T cells irradiated with 400 nm PDNPs, but not for the other photoporated groups. Also, a reduced TNFα production could be noted for 400 nm PDNPs at day 3 (**Figure S6**). The lower levels of cytokines are obviously biased by the lower cell density. Hence, we normalized the ELISA readouts to the cell numbers as determined by manual cell counting

(**Figure 6E**). After doing so, IFNγ levels in untreated and photoporated cultures were relatively similar, while the production of TNFα had increased for photo 400-treated cells, which may render T cells more susceptible to activation-induced cell death [71].

Importantly, the exposure to PDNPs without laser treatment had no measurable influence on cell proliferation and expression of activation markers (**Figure S7**), showing that the PDNPs by themselves do not affect T cell functionality.

Together, these data point to persistent phenotypic alterations of photo 400-treated T cells, resulting in diminished proliferation rates and aberrant expression of activation markers. On the contrary, T cells irradiated with smaller PDNPs preserved their propensity to become activated much better.

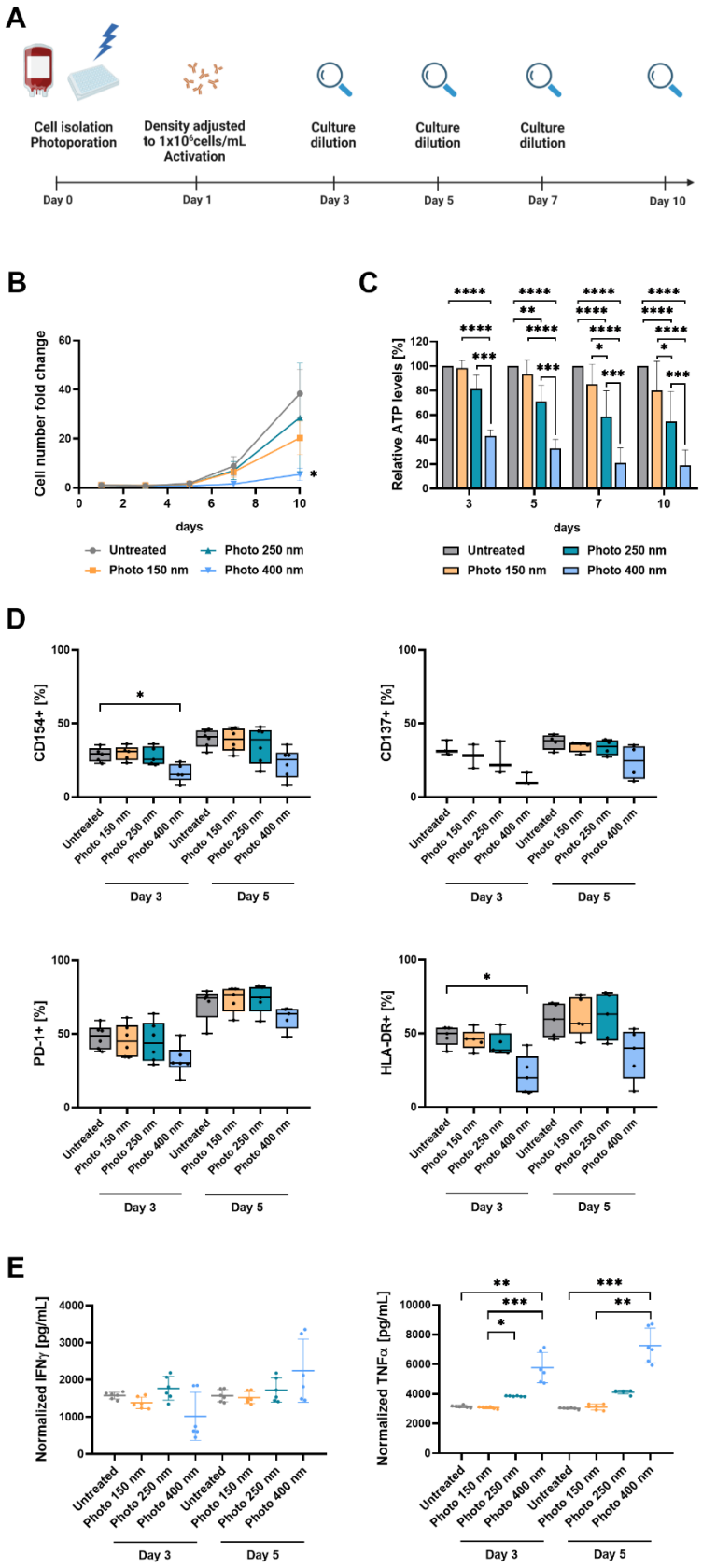
A
Cell isolation
Photoporation
Density adjusted
to 1x10⁶cells/mL
Activation
Culture
dilution
Culture
dilution
Culture
dilution
Day 0
Day 1
Day 3
Day 5
Day 7
Day 10
B
Cell number fold change
days
Untreated
Photo 150 nm
Photo 250 nm
Photo 400 nm
C
Relative ATP levels [%]
days
Untreated
Photo 150 nm
Photo 250 nm
Photo 400 nm
D
CD154+ [%]
CD137+ [%]
PD-1+ [%]
HLA-DR+ [%]
Untreated
Photo 150 nm
Photo 250 nm
Photo 400 nm
Day 3
Day 5
E
Normalized IFNγ [pg/mL]
Normalized TNFα [pg/mL]
Untreated
Photo 150 nm
Photo 250 nm
Photo 400 nm
Day 3
Day 5

537

Figure 6. Evaluation of T cell functionality after pre-treatment by PDNP photoporation.

(A) Schematic overview of the experimental setup and timeline (created with BioRender.com). Unstimulated T cells were treated by photoporation in the absence of FD500 on the day of isolation (day 0). The cells were then allowed to rest overnight. The next day (day 1), the cell density of every experimental group was adjusted to $1x10^6$ cells/mL to ensure the optimal stimulation with ImmunoCult CD3/CD28 T cell Activator, as per the manufacturer's instructions. Cultures were diluted at day 3, 5 and 7 and various experimental readouts were assayed at different time points. (B) Cell number fold changes in T cell cultures pre-treated with different PDNP sizes as assessed by cell counting with Trypan blue staining. The normalized cell growth was calculated relative to the seeding density at day 1. Data are represented as the mean ± SD of cultures of four different donors. Statistical analysis was performed using Two-way ANOVA with Tukey's multiple comparisons test (*$p < 0.05$). (C) Viability of T cell cultures was monitored using Cell Titer Glo assay. The values were calculated relative to the non-treated control at every time point. Data are represented as the mean ± SD of cultures of five different donors. Statistical analysis was performed using Two-way ANOVA with Tukey's multiple comparisons test (*$p < 0.05$; **$p < 0.01$; ***$p < 0.001$; ****$p < 0.0001$). (D) The expression of surface activation markers CD154, CD137, PD-1 and HLA-DR was evaluated by flow cytometry at day 3 and day 5 after the photoporation. Data are represented as boxes-and-whiskers showing the minimum to maximum results of cultures of at least three different donors. Statistical analysis was performed using Kruskal-Wallis nonparametric test with Dunn's multiple comparisons test (*$p < 0.05$). (E) The production of IFNγ and TNFα was determined using an ELISA assay. Cell culture supernatants were collected at day 3 and day 5 after the laser treatment. Results were normalized to the cell numbers determined by manual cell counting. Data are represented as the mean (center bar) ± SD of cultures of three different donors. Statistical analysis was performed using Kruskal-Wallis nonparametric test with Dunn's multiple comparisons test (*$p < 0.05$; **$p < 0.01$; ***$p < 0.001$).

4. Discussion

NP-mediated photoporation is a promising physical intracellular delivery technology, offering tunability and high throughput. Since it is a laser-activated method, it can deliver compounds in a spatiotemporally defined manner, even with single cell precision [72,73]. It has proven successful in the delivery of a wide range of molecules such as fluorescent markers [74,75], nucleic acids or proteins into various cell types including primary neurons [73] and T lymphocytes [39–41]. Recently, we demonstrated successful photoporation of cells using synthetic melanin-like nanoparticles as biodegradable replacement of the more commonly used inorganic nanoparticles, such as AuNPs [48]. These polydopamine nanoparticles (PDNPs) offer some unique advantages such as biocompatibility, biodegradability, synthesis from clinically approved precursors and excellent photothermal conversion properties over a broad spectral region [76–80].

In the field of CAR T cell therapies, vast research efforts have been directed towards increasing T cell potency and persistence *in vivo*. Recent evidence suggests that less differentiated cell phenotypes are preferred, so that *ex vivo* transfection of quiescent cells would be highly advantageous. It is, therefore, of crucial importance to select a delivery technology that minimally impacts the phenotype and functionality of T cells [26,81]. For instance, it was demonstrated that electroporation of T cells pushes them to an exhausted and therapeutically inferior phenotype [29,32,82], which is not the case for newer and gentler delivery technologies, such as microfluidic cell squeezing [32] and nanofiber-based photoporation [33].

To assess the value of PDNP photoporation for T cell engineering, it is, therefore, of importance to further investigate to which extent it can be used to deliver macromolecules in unstimulated T

583 cells without affecting the cell's phenotype. As activated T cells are larger than quiescent T cells
584 (**Figure 2**), we reasoned that it would be of interest to evaluate different sizes of PDNPs. Therefore,
585 we synthesized PDNPs with an average size of approximately 150 nm, 250 nm and 400 nm, which
586 were coated with BSA as before [48] to achieve good colloidal stability of PDNPs in Opti-MEM.
587 Importantly, human serum albumin (HAS) and bovine serum albumin (BSA) share several
588 characteristics, such as high solubility in water, long half-life in blood, similar molecular weight,
589 and a similar number of amino acid residues. Therefore, for (pre-clinical) research purposes, both
590 types of albumins have been widely applied, with no noticeable differences in properties of such
591 nanomaterials, suggesting that BSA can be substituted by HSA extracted from human blood at
592 later stages of technology translation [58–60].
593 Next, we optimized photoporation parameters for both unstimulated and expanded T cells by
594 extensive screening of PDNP concentrations and laser fluences. As a model cargo, we selected
595 FD500, which corresponds to a hydrodynamic diameter of 31 nm and falls in the size range of
596 some therapeutically relevant molecules, such as transcriptions factors, antibodies and genome-
597 editing nucleases [1]. In unstimulated T cells, we observed an inverse correlation between maximal
598 delivery yields and increasing PDNP sizes. 150 nm PDNPs significantly outperformed the largest
599 400 nm PD formulation, mainly due to inducing less toxicity for a similar delivery efficiency.
600 Importantly, optimal photoporation conditions for both 150 and 250 nm PDNPs were associated
601 with favorable viability above 70% and delivery efficiencies between 70 and 85%, resulting in a
602 delivery yield of 50-60%. However, when unstimulated cells were irradiated with 400 nm PDNPs,
603 cell viability dropped to ~55%, resulting in the lowest delivery yield among all tested formulations.
604 In the case of CD3/CD28 activated T cells, the overall best performance was obtained with 250
605 nm PDNPs, where high delivery efficiency (~90%) was combined with relatively low toxicity,

606 resulting in an excellent yield of ~70%. The delivery yield for both 150 and 400 nm PDNPs was
607 slightly less, although differences were not statistically significant. Altogether, slightly higher
608 delivery yields were achieved in pre-activated cells when compared to unstimulated T cells. This
609 was somehow expected and in agreement with previous studies on AuNP-mediated photoporation
610 which demonstrated that the efficiency of intracellular delivery increases with increasing cell size
611 [83]. Nonetheless, the delivery yield for both T cell models clearly exceeded those described
612 previously for FD500 delivery by AuNP-mediated photoporation in Jurkat cells (~20%) [84] and
613 PDNP-photoporation with 500 nm PDNPs in expanded T cells (~30%) [48]. This shows that, if
614 PDNP size is optimized for a given cell (pheno)type, they are excellent sensitizers for
615 photoporation, resulting in high delivery yields.

616 However, as discussed above, delivery efficiency alone is insufficient in the context of adoptive T
617 cell therapy, since also T cell fitness is a critical determinant of therapeutic efficacy. Therefore, to
618 better understand the functional implications of PDNP photoporation, we studied T cell propensity
619 to activation after laser exposure. We observed no significant changes to proliferation of photo
620 150 treated cells, indicating that T cells remained highly functional after treatment. Some impact
621 on growth rates could be noted after subculturing of photo 250-treated cells. However, expression
622 of activation markers and secretion of IFNγ and TNFα remained comparable to the untreated
623 control. In contrast, photo 400- treated T cells could not recover in terms of proliferation and
624 surface phenotype. These observations are in line with the ranking of PDNP size according to their
625 maximal delivery yields (150 nm > 250 nm > 400 nm), underscoring the importance of tailoring
626 the size of the photosensitizer to a specific cell (pheno)type to ensure optimal delivery and cell
627 phenotype preservation.

The reason why larger PDNPs have a bigger impact on small quiescent T cells can be due to two reasons. First of all, for the laser fluences used in this study, the 150 nm PDNPs did not generate VNB, meaning that membrane pore formation was due to direct heating. Instead, 400 nm PDNPs did form VNB, in which case pores are generated by a different mechanism (mechanical perturbation). Therefore, it could be that VNB formation by larger PDNPs, and the mechanical pressure waves that result from that, inflict more damage to cells as compared to mere heating at the plasma membrane. A second reason could be that VNB formation by large PDNPs results in larger membrane pores, which could be more difficult to repair by small cells like unstimulated T cells [85,86]. In any case, whatever the underlying reason, this perturbation resulted in immediate cell loss as demonstrated by ATP measurements performed 2 hours after laser treatment. Additionally, the surviving cell population carried some persistent phenotype alterations which manifested themselves in reduced proliferation rates during *in vitro* expansion. Moreover, we observed an aberrant cytokine production, similar to what was reported before for the treatment by electroporation [32,33].

Having identified PDNP sizes that have a minimal impact on T cell activation propensity, in future work it will be of interest to determine delivery efficiency in different T cell subsets, such as naïve or memory cells and analyze the impact of photoporation treatment on the respective subpopulations, for instance by single cell sequencing. Such phenotypical analysis could reveal more about the impact of PDNP photoporation on T cell differentiation. Lastly, the investigation of T cell functionality may be strengthened by the assessment of antigen specific cytolytic activity of photoporated CAR-T cells as has been done before for nanofiber photoporation [33]. Nonetheless, the multiparametric *in vitro* analysis performed in this study provides valuable

insights for further optimization of PDNP photoporation towards genetic engineering of highly functional human T cells.

5. Conclusion

In summary, we optimized PDNP photoporation for macromolecule delivery in both unstimulated and expanded human T cells. A systematic screening of photosensitizer sizes revealed that laser treatment of quiescent cells with small 150 nm PDNPs generates favorable delivery yields with a minimal impact on T cell functionality. Our findings highlight the need for tailoring the size of photothermal NPs to cell (pheno)type and the importance of careful evaluation the effect of the delivery method on phenotype and functionality. The observations made in this study will be helpful to further develop photoporation as an intracellular delivery method for the genetic engineering of clinically relevant immune cells.

Author contributions

Conceptualization: D.B., W.H.D.V. and K.B. Investigation: D.B., A.H., I.G., G.G., S.D.M, D.P., H.D.K., and V.B. Formal analysis and Visualization: D.B. Resources: G.G. Writing – original draft: DB. Writing – review & editing: D.B., A.H., I.G., G.G., S.D.M, D.P., H.D.K., V.B, P.D., B.V., S.C.D.S., W.H.D.V. and K.B. Funding acquisition: W.H.D.V. and K.B. Supervision: P.D., B.V, S.C.D.S., W.H.D.V. and K.B.

Declaration of competing interests

The authors declare no competing interests.

Acknowledgements

The authors would like to thank Olivier Janssen for the acquisition of the SEM images of polydopamine nanoparticles and Ghent Light Microscopy Core at Ghent University (Belgium) for the use and support of confocal microscopy experiments.

FUNDING

The authors acknowledge with gratitude funding by the Flemish Research Fund (grant G005819; I003420N; I000321N; G033322N), The University of Antwerp (grant IOF46415; BOF41739; BOF43015) and the European Research Council (Proof of Concept Grant INTRACYTE).

References

[1] M.P. Stewart, R. Langer, K.F. Jensen, Intracellular delivery by membrane disruption: Mechanisms, strategies, and concepts, Chem. Rev. 118 (2018) 7409–7531. https://doi.org/10.1021/acs.chemrev.7b00678.

[2] M. Sadelain, I. Rivière, S. Riddell, Therapeutic T cell engineering, Nature. 545 (2017) 423–431. https://doi.org/10.1038/nature22395.

[3] R.G. Majzner, C.L. Mackall, Clinical lessons learned from the first leg of the CAR T cell journey, Nat. Med. 25 (2019) 1341–1355. https://doi.org/10.1038/s41591-019-0564-6.

[4] A.D. Waldman, J.M. Fritz, M.J. Lenardo, A guide to cancer immunotherapy: from T cell basic science to clinical practice, Nat. Rev. Immunol. 20 (2020) 651–668. https://doi.org/10.1038/s41577-020-0306-5.

[5] S.L. Maude, N. Frey, P.A. Shaw, R. Aplenc, D.M. Barrett, N.J. Bunin, A. Chew, V.E. Gonzalez, Z. Zheng, S.F. Lacey, Y.D. Mahnke, J.J. Melenhorst, S.R. Rheingold, A. Shen, D.T. Teachey, B.L. Levine, C.H. June, D.L. Porter, S.A. Grupp, Chimeric Antigen Receptor T Cells for Sustained Remissions in Leukemia, N. Engl. J. Med. 371 (2014) 1507–1517. https://doi.org/10.1056/nejmoa1407222.

[6] J.H. Park, I. Rivière, M. Gonen, X. Wang, B. Sénéchal, K.J. Curran, C. Sauter, Y. Wang, B. Santomasso, E. Mead, M. Roshal, P. Maslak, M. Davila, R.J. Brentjens, M. Sadelain, Long-Term Follow-up of CD19 CAR Therapy in Acute Lymphoblastic Leukemia, N. Engl. J. Med. 378 (2018) 449–459. https://doi.org/10.1056/nejmoa1709919.

[7] S.L. Maude, T.W. Laetsch, J. Buechner, S. Rives, M. Boyer, H. Bittencourt, P. Bader, M.R. Verneris, H.E. Stefanski, G.D. Myers, M. Qayed, B. De Moerloose, H. Hiramatsu, K. Schlis, K.L. Davis, P.L. Martin, E.R. Nemecek, G.A. Yanik, C. Peters, A. Baruchel, N. Boissel, F. Mechinaud, A. Balduzzi, J. Krueger, C.H. June, B.L. Levine, P. Wood, T. Taran, M. Leung, K.T. Mueller, Y. Zhang, K. Sen, D. Lebwohl, M.A. Pulsipher, S.A. Grupp, Tisagenlecleucel in Children and Young Adults with B-Cell Lymphoblastic Leukemia, N. Engl. J. Med. 378 (2018) 439–448. https://doi.org/10.1056/nejmoa1709866.

[8] S.S. Neelapu, F.L. Locke, N.L. Bartlett, L.J. Lekakis, D.B. Miklos, C.A. Jacobson, I. Braunschweig, O.O. Oluwole, T. Siddiqi, Y. Lin, J.M. Timmerman, P.J. Stiff, J.W. Friedberg, I.W. Flinn, A. Goy, B.T. Hill, M.R. Smith, A. Deol, U. Farooq, P. McSweeney, J. Munoz, I. Avivi, J.E. Castro, J.R. Westin, J.C. Chavez, A. Ghobadi, K. V. Komanduri, R. Levy, E.D. Jacobsen, T.E. Witzig, P. Reagan, A. Bot, J. Rossi, L. Navale, Y. Jiang, J. Aycock, M. Elias, D. Chang, J. Wiezorek, W.Y. Go, Axicabtagene Ciloleucel CAR T-Cell Therapy in Refractory Large B-Cell Lymphoma, N. Engl. J. Med. 377 (2017) 2531–2544. https://doi.org/10.1056/nejmoa1707447.

[9] F.L. Locke, A. Ghobadi, C.A. Jacobson, D.B. Miklos, L.J. Lekakis, O.O. Oluwole, Y. Lin, I. Braunschweig, B.T. Hill, J.M. Timmerman, A. Deol, P.M. Reagan, P. Stiff, I.W. Flinn, U. Farooq, A. Goy, P.A. McSweeney, J. Munoz, T. Siddiqi, J.C. Chavez, A.F. Herrera, N.L. Bartlett, J.S. Wiezorek, L. Navale, A. Xue, Y. Jiang, A. Bot, J.M. Rossi, J.J. Kim, W.Y. Go, S.S. Neelapu, Long-term safety and activity of axicabtagene ciloleucel in refractory large B-cell lymphoma (ZUMA-1): a single-arm, multicentre, phase 1–2 trial, Lancet Oncol. 20 (2019) 31–42. https://doi.org/10.1016/S1470-2045(18)30864-7.

[10] L. Gattinoni, C.A. Klebanoff, D.C. Palmer, C. Wrzesinski, K. Kerstann, Z. Yu, S.E. Finkelstein, M.R. Theoret, S.A. Rosenberg, N.P. Restifo, Acquisition of full effector function in vitro paradoxically impairs the in vivo antitumor efficacy of adoptively transferred CD8+ T cells, J. Clin. Invest. 115 (2005) 1616–1626. https://doi.org/10.1172/JCI24480.

[11] C.A. Klebanoff, L. Gattinoni, P. Torabi-Parizi, K. Kerstann, A.R. Cardones, S.E. Finkelstein, D.C. Palmer, P.A. Antony, S.T. Hwang, S.A. Rosenberg, T.A. Waldmann, N.P. Restifo, Central memory self/tumor-reactive CD8+ T cells confer superior antitumor

immunity compared with effector memory T cells, Proc. Natl. Acad. Sci. U. S. A. 102 (2005) 9571–9576. https://doi.org/10.1073/pnas.0503726102.

[12] C.S. Hinrichs, Z.A. Borman, L. Cassard, L. Gattinoni, R. Spolski, Y. Zhiya, L. Sanchez-Perez, P. Muranski, S.J. Kern, C. Logun, D.C. Palmer, J. Yun, R.N. Reger, W.J. Leonard, R.L. Danner, S.A. Rosenberg, N.P. Restifo, Adoptively transferred effector cells derived from naïve rather than central memory CD8+ T cells mediate superior antitumor immunity, Proc. Natl. Acad. Sci. U. S. A. 106 (2009) 17469–17474. https://doi.org/10.1073/pnas.0907448106.

[13] L. Gattinoni, E. Lugli, Y. Ji, Z. Pos, C.M. Paulos, M.F. Quigley, J.R. Almeida, E. Gostick, Z. Yu, C. Carpenito, E. Wang, D.C. Douek, D.A. Price, C.H. June, F.M. Marincola, M. Roederer, N.P. Restifo, A human memory T cell subset with stem cell–like properties, Nat. Med. 17 (2011) 1290–1297. https://doi.org/10.1038/nm.2446.

[14] J.A. Fraietta, C.L. Nobles, M.A. Sammons, S. Lundh, S.A. Carty, T.J. Reich, A.P. Cogdill, J.J.D. Morrissette, J.E. DeNizio, S. Reddy, Y. Hwang, M. Gohil, I. Kulikovskaya, F. Nazimuddin, M. Gupta, F. Chen, J.K. Everett, K.A. Alexander, E. Lin-Shiao, M.H. Gee, X. Liu, R.M. Young, D. Ambrose, Y. Wang, J. Xu, M.S. Jordan, K.T. Marcucci, B.L. Levine, K.C. Garcia, Y. Zhao, M. Kalos, D.L. Porter, R.M. Kohli, S.F. Lacey, S.L. Berger, F.D. Bushman, C.H. June, J.J. Melenhorst, Disruption of TET2 promotes the therapeutic efficacy of CD19-targeted T cells, Nature. 558 (2018) 307–312. https://doi.org/10.1038/s41586-018-0178-z.

[15] J.A. Fraietta, S.F. Lacey, E.J. Orlando, I. Pruteanu-Malinici, M. Gohil, S. Lundh, A.C. Boesteanu, Y. Wang, R.S. O'connor, W.T. Hwang, E. Pequignot, D.E. Ambrose, C. Zhang, N. Wilcox, F. Bedoya, C. Dorfmeier, F. Chen, L. Tian, H. Parakandi, M. Gupta,

R.M. Young, F.B. Johnson, I. Kulikovskaya, L. Liu, J. Xu, S.H. Kassim, M.M. Davis, B.L. Levine, N. V. Frey, D.L. Siegel, A.C. Huang, E.J. Wherry, H. Bitter, J.L. Brogdon, D.L. Porter, C.H. June, J.J. Melenhorst, Determinants of response and resistance to CD19 chimeric antigen receptor (CAR) T cell therapy of chronic lymphocytic leukemia, Nat. Med. 24 (2018) 563–571. https://doi.org/10.1038/s41591-018-0010-1.

[16] S. Arcangeli, L. Falcone, B. Camisa, F. De Girardi, M. Biondi, F. Giglio, F. Ciceri, C. Bonini, A. Bondanza, M. Casucci, Next-Generation Manufacturing Protocols Enriching TSCM CAR T Cells Can Overcome Disease-Specific T Cell Defects in Cancer Patients, Front. Immunol. 11 (2020). https://doi.org/10.3389/fimmu.2020.01217.

[17] S. Ghassemi, S. Nunez-Cruz, R.S. O'Connor, J.A. Fraietta, P.R. Patel, J. Scholler, D.M. Barrett, S.M. Lundh, M.M. Davis, F. Bedoya, C. Zhang, J. Leferovich, S.F. Lacey, B.L. Levine, S.A. Grupp, C.H. June, J.J. Melenhorst, M.C. Milone, Reducing ex vivo culture improves the antileukemic activity of chimeric antigen receptor (CAR) T cells, Cancer Immunol. Res. 6 (2018) 1100–1109. https://doi.org/10.1158/2326-6066.CIR-17-0405.

[18] S. Ghassemi, J.S. Durgin, S. Nunez-Cruz, J. Patel, J. Leferovich, M. Pinzone, F. Shen, K.D. Cummins, G. Plesa, V.A. Cantu, S. Reddy, F.D. Bushman, S.I. Gill, U. O'Doherty, R.S. O'Connor, M.C. Milone, Rapid manufacturing of non-activated potent CAR T cells, Nat. Biomed. Eng. 6 (2022) 118–128. https://doi.org/10.1038/s41551-021-00842-6.

[19] L. de Macedo Abdo, L.R.C. Barros, M. Saldanha Viegas, L. Vieira Codeço Marques, P. de Sousa Ferreira, L. Chicaybam, M.H. Bonamino, Development of CAR-T cell therapy for B-ALL using a point-of-care approach, Oncoimmunology. 9 (2020). https://doi.org/10.1080/2162402X.2020.1752592.

[20] L. Liu, C. Johnson, S. Fujimura, F. Teque, J.A. Levy, Transfection optimization for

primary human CD8+ cells, J. Immunol. Methods. 372 (2011) 22–29. https://doi.org/10.1016/j.jim.2011.06.026.

[21] A. Seki, S. Rutz, Optimized RNP transfection for highly efficient CRI SPR/Cas9-mediated gene knockout in primary T cells, J. Exp. Med. 215 (2018) 985–997. https://doi.org/10.1084/jem.20171626.

[22] P. Aksoy, B.A. Aksoy, E. Czech, J. Hammerbacher, Viable and efficient electroporation-based genetic manipulation of unstimulated human T cells, BioRxiv. (2018) 1–34. https://doi.org/10.1101/466243.

[23] P. Vormittag, R. Gunn, S. Ghorashian, F.S. Veraitch, A guide to manufacturing CAR T cell therapies, Curr. Opin. Biotechnol. 53 (2018) 164–181. https://doi.org/10.1016/j.copbio.2018.01.025.

[24] J.E. Eyles, S. Vessillier, A. Jones, G. Stacey, C.K. Schneider, J. Price, Cell therapy products: focus on issues with manufacturing and quality control of chimeric antigen receptor T-cell therapies, J. Chem. Technol. Biotechnol. 94 (2019) 1008–1016. https://doi.org/10.1002/jctb.5829.

[25] B.L. Levine, J. Miskin, K. Wonnacott, C. Keir, Global Manufacturing of CAR T Cell Therapy, Mol. Ther. - Methods Clin. Dev. 4 (2017) 92–101. https://doi.org/10.1016/j.omtm.2016.12.006.

[26] L. Raes, S.C. De Smedt, K. Raemdonck, K. Braeckmans, Non-viral transfection technologies for next-generation therapeutic T cell engineering, Biotechnol. Adv. 49 (2021) 107760. https://doi.org/10.1016/j.biotechadv.2021.107760.

[27] A. Moretti, M. Ponzo, C.A. Nicolette, I.Y. Tcherepanova, A. Biondi, C.F. Magnani, The Past, Present, and Future of Non-Viral CAR T Cells, Front. Immunol. 13 (2022) 1–25.

https://doi.org/10.3389/fimmu.2022.867013.

[28] D.L. Wagner, U. Koehl, M. Chmielewski, C. Scheid, R. Stripecke, Review: Sustainable Clinical Development of CAR-T Cells – Switching From Viral Transduction Towards CRISPR-Cas Gene Editing, Front. Immunol. 13 (2022) 1–13. https://doi.org/10.3389/fimmu.2022.865424.

[29] S. Huerfano, B. Ryabchenko, J. Forstová, Nucleofection of Expression Vectors Induces a Robust Interferon Response and Inhibition of Cell Proliferation, DNA Cell Biol. 32 (2013) 467–479. https://doi.org/10.1089/dna.2012.1950.

[30] M.K. Cromer, S. Vaidyanathan, D.E. Ryan, B. Curry, A.B. Lucas, J. Camarena, M. Kaushik, S.R. Hay, R.M. Martin, I. Steinfeld, R.O. Bak, D.P. Dever, A. Hendel, L. Bruhn, M.H. Porteus, Global Transcriptional Response to CRISPR/Cas9-AAV6-Based Genome Editing in CD34+ Hematopoietic Stem and Progenitor Cells, Mol. Ther. 26 (2018) 2431–2442. https://doi.org/10.1016/j.ymthe.2018.06.002.

[31] A. Tay, N. Melosh, Transfection with Nanostructure Electro-Injection is Minimally Perturbative, Adv. Ther. 2 (2019) 1900133. https://doi.org/10.1002/adtp.201900133.

[32] T. DiTommaso, J.M. Cole, L. Cassereau, J.A. Buggé, J.L.S. Hanson, D.T. Bridgen, B.D. Stokes, S.M. Loughhead, B.A. Beutel, J.B. Gilbert, K. Nussbaum, A. Sorrentino, J. Toggweiler, T. Schmidt, G. Gyuelveszi, H. Bernstein, A. Sharei, Cell engineering with microfluidic squeezing preserves functionality of primary immune cells in vivo, Proc. Natl. Acad. Sci. 115 (2018) E10907–E10914. https://doi.org/10.1073/pnas.1809671115.

[33] R. Xiong, D. Hua, J. Van Hoeck, D. Berdecka, L. Léger, S. De Munter, J.C. Fraire, L. Raes, A. Harizaj, F. Sauvage, G. Goetgeluk, M. Pille, J. Aalders, J. Belza, T. Van Acker, E. Bolea-Fernandez, T. Si, F. Vanhaecke, W.H. De Vos, B. Vandekerckhove, J. van

824 Hengel, K. Raemdonck, C. Huang, S.C. De Smedt, K. Braeckmans, Photothermal
825 nanofibres enable safe engineering of therapeutic cells, Nat. Nanotechnol. 16 (2021)
826 1281–1291. https://doi.org/10.1038/s41565-021-00976-3.
827 [34] R. Xiong, S.K. Samal, J. Demeester, A.G. Skirtach, S.C. De Smedt, K. Braeckmans,
828 Laser-assisted photoporation: fundamentals, technological advances and applications,
829 Adv. Phys. X. 1 (2016) 596–620. https://doi.org/10.1080/23746149.2016.1228476.
830 [35] J. Ramon, R. Xiong, S.C. De Smedt, K. Raemdonck, K. Braeckmans, Vapor nanobubble-
831 mediated photoporation constitutes a versatile intracellular delivery technology, Curr.
832 Opin. Colloid Interface Sci. 54 (2021) 101453.
833 https://doi.org/10.1016/j.cocis.2021.101453.
834 [36] A.S. Urban, M. Fedoruk, M.R. Horton, J.O. Rädler, F.D. Stefani, J. Feldmann, Controlled
835 nanometric phase transitions of phospholipid membranes by plasmonic heating of single
836 gold nanoparticles, Nano Lett. 9 (2009) 2903–2908. https://doi.org/10.1021/nl901201h.
837 [37] R. Xiong, K. Raemdonck, K. Peynshaert, I. Lentacker, I. De Cock, J. Demeester, S.C. De
838 Smedt, A.G. Skirtach, K. Braeckmans, Comparison of gold nanoparticle mediated
839 photoporation: Vapor nanobubbles outperform direct heating for delivering
840 macromolecules in live cells, ACS Nano. 8 (2014) 6288–6296.
841 https://doi.org/10.1021/nn5017742.
842 [38] E. Lukianova-Hleb, Y. Hu, L. Latterini, L. Tarpani, S. Lee, R.A. Drezek, J.H. Hafner,
843 D.O. Lapotko, Plasmonic nanobubbles as transient vapor nanobubbles generated around
844 plasmonic nanoparticles, ACS Nano. 4 (2010) 2109–2123.
845 https://doi.org/10.1021/nn1000222.
846 [39] L. Wayteck, R. Xiong, K. Braeckmans, S.C. De Smedt, K. Raemdonck, Comparing

847 photoporation and nucleofection for delivery of small interfering RNA to cytotoxic T
848 cells, J. Control. Release. 267 (2017) 154–162.
849 https://doi.org/10.1016/j.jconrel.2017.08.002.
850 [40] L. Raes, S. Stremersch, J.C. Fraire, T. Brans, G. Goetgeluk, S. De Munter, L. Van
851 Hoecke, R. Verbeke, J. Van Hoeck, R. Xiong, X. Saelens, B. Vandekerckhove, S. De
852 Smedt, K. Raemdonck, K. Braeckmans, Intracellular Delivery of mRNA in Adherent and
853 Suspension Cells by Vapor Nanobubble Photoporation, Nano-Micro Lett. 12 (2020) 1–17.
854 https://doi.org/10.1007/s40820-020-00523-0.
855 [41] L. Raes, M. Pille, A. Harizaj, G. Goetgeluk, J. Van Hoeck, S. Stremersch, J.C. Fraire, T.
856 Brans, O.G. de Jong, R. Maas-Bakker, E. Mastrobattista, P. Vader, S.C. De Smedt, B.
857 Vandekerckhove, K. Raemdonck, K. Braeckmans, Cas9 RNP transfection by vapor
858 nanobubble photoporation for ex vivo cell engineering, Mol. Ther. - Nucleic Acids. 25
859 (2021) 696–707. https://doi.org/10.1016/j.omtn.2021.08.014.
860 [42] G. Bongiovanni, P.K. Olshin, C. Yan, J.M. Voss, M. Drabbels, U.J. Lorenz, The
861 fragmentation mechanism of gold nanoparticles in water under femtosecond laser
862 irradiation, Nanoscale Adv. 3 (2021) 5277–5283. https://doi.org/10.1039/d1na00406a.
863 [43] G. González-Rubio, A. Guerrero-Martínez, L.M. Liz-Marzán, Reshaping, Fragmentation,
864 and Assembly of Gold Nanoparticles Assisted by Pulse Lasers, Acc. Chem. Res. 49
865 (2016) 678–686. https://doi.org/10.1021/acs.accounts.6b00041.
866 [44] A.R. Ziefuss, S. Reich, S. Reichenberger, M. Levantino, A. Plech, In situ structural
867 kinetics of picosecond laser-induced heating and fragmentation of colloidal gold spheres,
868 Phys. Chem. Chem. Phys. 22 (2020) 4993–5001. https://doi.org/10.1039/c9cp05202j.
869 [45] M. Tsoli, H. Kuhn, W. Brandau, H. Esche, G. Schmid, Cellular uptake and toxicity of

Au55 clusters, Small. 1 (2005) 841–844. https://doi.org/10.1002/smll.200500104.

[46] Y. Pan, S. Neuss, A. Leifert, M. Fischler, F. Wen, U. Simon, G. Schmid, W. Brandau, W. Jahnen-Dechent, Size-dependent cytotoxicity of gold nanoparticles, Small. 3 (2007) 1941–1949. https://doi.org/10.1002/smll.200700378.

[47] J.H. Ryu, P.B. Messersmith, H. Lee, Polydopamine Surface Chemistry: A Decade of Discovery, ACS Appl. Mater. Interfaces. 10 (2018) 7523–7540. https://doi.org/10.1021/acsami.7b19865.

[48] A. Harizaj, M. Wels, L. Raes, S. Stremersch, G. Goetgeluk, T. Brans, B. Vandekerckhove, F. Sauvage, S.C. De Smedt, I. Lentacker, K. Braeckmans, Photoporation with Biodegradable Polydopamine Nanosensitizers Enables Safe and Efficient Delivery of mRNA in Human T Cells, Adv. Funct. Mater. 31 (2021) 2102472. https://doi.org/10.1002/adfm.202102472.

[49] J. Schindelin, I. Arganda-Carreras, E. Frise, V. Kaynig, M. Longair, T. Pietzsch, S. Preibisch, C. Rueden, S. Saalfeld, B. Schmid, J.-Y. Tinevez, D.J. White, V. Hartenstein, K. Eliceiri, P. Tomancak, A. Cardona, Fiji: an open-source platform for biological-image analysis, Nat. Methods. 9 (2012) 676–682. https://doi.org/10.1038/nmeth.2019.

[50] K.Y. Ju, Y. Lee, S. Lee, S.B. Park, J.K. Lee, Bioinspired polymerization of dopamine to generate melanin-like nanoparticles having an excellent free-radical-scavenging property, Biomacromolecules. 12 (2011) 625–632. https://doi.org/10.1021/bm101281b.

[51] V. Filipe, A. Hawe, W. Jiskoot, Critical evaluation of nanoparticle tracking analysis (NTA) by NanoSight for the measurement of nanoparticles and protein aggregates, Pharm. Res. 27 (2010) 796–810. https://doi.org/10.1007/s11095-010-0073-2.

[52] R.D. Boyd, S.K. Pichaimuthu, A. Cuenat, New approach to inter-technique comparisons

for nanoparticle size measurements; using atomic force microscopy, nanoparticle tracking analysis and dynamic light scattering, Colloids Surfaces A Physicochem. Eng. Asp. 387 (2011) 35–42. https://doi.org/10.1016/j.colsurfa.2011.07.020.

[53] J. Shang, X. Gao, Nanoparticle counting: towards accurate determination of the molar concentration, Chem. Soc. Rev. 43 (2014) 7267–7278. https://doi.org/10.1039/C4CS00128A.

[54] N. Nishizawa, A. Kawamura, M. Kohri, Y. Nakamura, S. Fujii, Polydopamine Particle as a Particulate Emulsifier, Polymers (Basel). 8 (2016) 62. https://doi.org/10.3390/polym8030062.

[55] T. Wolf, W. Jin, G. Zoppi, I.A. Vogel, M. Akhmedov, C.K.E. Bleck, T. Beltraminelli, J.C. Rieckmann, N.J. Ramirez, M. Benevento, S. Notarbartolo, D. Bumann, F. Meissner, B. Grimbacher, M. Mann, A. Lanzavecchia, F. Sallusto, I. Kwee, R. Geiger, Dynamics in protein translation sustaining T cell preparedness, Nat. Immunol. 21 (2020) 927–937. https://doi.org/10.1038/s41590-020-0714-5.

[56] A.J.M. Howden, J.L. Hukelmann, A. Brenes, L. Spinelli, L. V. Sinclair, A.I. Lamond, D.A. Cantrell, Quantitative analysis of T cell proteomes and environmental sensors during T cell differentiation, Nat. Immunol. 20 (2019) 1542–1554. https://doi.org/10.1038/s41590-019-0495-x.

[57] X. Wang, Z. Chen, P. Yang, J. Hu, Z. Wang, Y. Li, Size control synthesis of melanin-like polydopamine nanoparticles by tuning radicals, Polym. Chem. 10 (2019) 4194–4200. https://doi.org/10.1039/C9PY00517J.

[58] Z. Liu, X. Chen, Simple bioconjugate chemistry serves great clinical advances: albumin as a versatile platform for diagnosis and precision therapy, Chem. Soc. Rev. 45 (2016) 1432–

916 1456. https://doi.org/10.1039/C5CS00158G.
917 [59] F.-F. An, X.-H. Zhang, Strategies for Preparing Albumin-based Nanoparticles for
918 Multifunctional Bioimaging and Drug Delivery, Theranostics. 7 (2017) 3667–3689.
919 https://doi.org/10.7150/thno.19365.
920 [60] B. Ghalandari, Y. Yu, F. Ghorbani, A.R. Warden, K.Z. Ahmad, X. Sang, S. Huang, Y.
921 Zhang, W. Su, A. Divsalar, X. Ding, Polydopamine nanospheres coated with bovine
922 serum albumin permit enhanced cell differentiation: fundamental mechanism and practical
923 application for protein coating formation, Nanoscale. 13 (2021) 20098–20110.
924 https://doi.org/10.1039/D1NR07469E.
925 [61] H. Lee, J. Rho, P.B. Messersmith, Facile Conjugation of Biomolecules onto Surfaces via
926 Mussel Adhesive Protein Inspired Coatings, Adv. Mater. 21 (2009) 431–434.
927 https://doi.org/10.1002/adma.200801222.
928 [62] J. Liu, H. Xu, X. Tang, J. Xu, Z. Jin, H. Li, S. Wang, J. Gou, X. Jin, Simple and tunable
929 surface coatings via polydopamine for modulating pharmacokinetics, cell uptake and
930 biodistribution of polymeric nanoparticles, RSC Adv. 7 (2017) 15864–15876.
931 https://doi.org/10.1039/C7RA01354J.
932 [63] N. Singh, J. Nayak, K. Patel, S.K. Sahoo, R. Kumar, Electrochemical impedance
933 spectroscopy reveals a new mechanism based on competitive binding between Tris and
934 protein on a conductive biomimetic polydopamine surface, Phys. Chem. Chem. Phys. 20
935 (2018) 25812–25821. https://doi.org/10.1039/C8CP05391J.
936 [64] V.S. Raghuwanshi, B. Yu, C. Browne, G. Garnier, Reversible pH Responsive Bovine
937 Serum Albumin Hydrogel Sponge Nanolayer, Front. Bioeng. Biotechnol. 8 (2020) 1–10.
938 https://doi.org/10.3389/fbioe.2020.00573.

[65] R. Purohit, N.S. Vallabani, R.K. Shukla, A. Kumar, S. Singh, Effect of gold nanoparticle size and surface coating on human red blood cells, Bioinspired, Biomim. Nanobiomaterials. 5 (2016) 121–131. https://doi.org/10.1680/jbibn.15.00018.

[66] T. Mudalige, H. Qu, D. Van Haute, S.M. Ansar, A. Paredes, T. Ingle, Characterization of Nanomaterials, in: Nanomater. Food Appl., Elsevier, 2019: pp. 313–353. https://doi.org/10.1016/B978-0-12-814130-4.00011-7.

[67] M. Danaei, M. Dehghankhold, S. Ataei, F. Hasanzadeh Davarani, R. Javanmard, A. Dokhani, S. Khorasani, M. Mozafari, Impact of Particle Size and Polydispersity Index on the Clinical Applications of Lipidic Nanocarrier Systems, Pharmaceutics. 10 (2018) 57. https://doi.org/10.3390/pharmaceutics10020057.

[68] A. Caruso, S. Licenziati, M. Corulli, A.D. Canaris, M.A. De Francesco, S. Fiorentini, L. Peroni, F. Fallacara, F. Dima, A. Balsari, A. Turano, Flow cytometric analysis of activation markers on stimulated T cells and their correlation with cell proliferation, Cytometry. 27 (1997) 71–76. https://doi.org/10.1002/(SICI)1097-0320(19970101)27:1<71::AID-CYTO9>3.0.CO;2-O.

[69] M. Reddy, E. Eirikis, C. Davis, H.M. Davis, U. Prabhakar, Comparative analysis of lymphocyte activation marker expression and cytokine secretion profile in stimulated human peripheral blood mononuclear cell cultures: An in vitro model to monitor cellular immune function, J. Immunol. Methods. 293 (2004) 127–142. https://doi.org/10.1016/j.jim.2004.07.006.

[70] M. Shipkova, E. Wieland, Surface markers of lymphocyte activation and markers of cell proliferation, Clin. Chim. Acta. 413 (2012) 1338–1349. https://doi.org/10.1016/j.cca.2011.11.006.

[71] I. Popescu, M.E. Snyder, C.J. Iasella, S.J. Hannan, R. Koshy, R. Burke, A. Das, M.J. Brown, E.J. Lyons, S.C. Lieber, X. Chen, J.C. Sembrat, P. Bhatt, E. Deng, X. An, K. Linstrum, G. Kitsios, I. Konstantinidis, M. Saul, D.J. Kass, J.K. Alder, B.B. Chen, E.A. Lendermon, S. Kilaru, B. Johnson, J.M. Pilewski, J.E. Kiss, A.H. Wells, A. Morris, B.J. McVerry, D.K. McMahon, D.J. Triulzi, K. Chen, P.G. Sanchez, J.F. McDyer, CD4 + T-Cell Dysfunction in Severe COVID-19 Disease Is Tumor Necrosis Factor-α/Tumor Necrosis Factor Receptor 1–Dependent, Am. J. Respir. Crit. Care Med. 205 (2022) 1403–1418. https://doi.org/10.1164/rccm.202111-2493OC.

[72] R. Xiong, C. Drullion, P. Verstraelen, J. Demeester, A.G. Skirtach, C. Abbadie, W.H. De Vos, S.C. De Smedt, K. Braeckmans, Fast spatial-selective delivery into live cells, J. Control. Release. 266 (2017) 198–204. https://doi.org/10.1016/j.jconrel.2017.09.033.

[73] R. Xiong, P. Verstraelen, J. Demeester, A.G. Skirtach, J.-P. Timmermans, S.C. De Smedt, W.H. De Vos, K. Braeckmans, Selective Labeling of Individual Neurons in Dense Cultured Networks With Nanoparticle-Enhanced Photoporation, Front. Cell. Neurosci. 12 (2018) 1–11. https://doi.org/10.3389/fncel.2018.00080.

[74] R. Xiong, F. Joris, S. Liang, R. De Rycke, S. Lippens, J. Demeester, A. Skirtach, K. Raemdonck, U. Himmelreich, S.C. De Smedt, K. Braeckmans, Cytosolic Delivery of Nanolabels Prevents Their Asymmetric Inheritance and Enables Extended Quantitative in Vivo Cell Imaging, Nano Lett. 16 (2016) 5975–5986. https://doi.org/10.1021/acs.nanolett.6b01411.

[75] J. Liu, R. Xiong, T. Brans, S. Lippens, E. Parthoens, F.C. Zanacchi, R. Magrassi, S.K. Singh, S. Kurungot, S. Szunerits, H. Bové, M. Ameloot, J.C. Fraire, E. Teirlinck, S.K. Samal, R. De Rycke, G. Houthaeve, S.C. De Smedt, R. Boukherroub, K. Braeckmans,

Repeated photoporation with graphene quantum dots enables homogeneous labeling of live cells with extrinsic markers for fluorescence microscopy, Light Sci. Appl. 7 (2018). https://doi.org/10.1038/s41377-018-0048-3.

[76] S.H. Ku, C.B. Park, Human endothelial cell growth on mussel-inspired nanofiber scaffold for vascular tissue engineering, Biomaterials. 31 (2010) 9431–9437. https://doi.org/10.1016/j.biomaterials.2010.08.071.

[77] Y. Liu, K. Ai, J. Liu, M. Deng, Y. He, L. Lu, Dopamine-melanin colloidal nanospheres: An efficient near-infrared photothermal therapeutic agent for in vivo cancer therapy, Adv. Mater. 25 (2013) 1353–1359. https://doi.org/10.1002/adma.201204683.

[78] X. Liu, J. Cao, H. Li, J. Li, Q. Jin, K. Ren, J. Ji, Mussel-inspired polydopamine: A biocompatible and ultrastable coating for nanoparticles in vivo, ACS Nano. 7 (2013) 9384–9395. https://doi.org/10.1021/nn404117j.

[79] B. Poinard, S.A.E. Lam, K.G. Neoh, J.C.Y. Kah, Mucopenetration and biocompatibility of polydopamine surfaces for delivery in an Ex Vivo porcine bladder, J. Control. Release. 300 (2019) 161–173. https://doi.org/10.1016/j.jconrel.2019.02.041.

[80] A. Carmignani, M. Battaglini, E. Sinibaldi, A. Marino, V. Vighetto, V. Cauda, G. Ciofani, In Vitro and Ex Vivo Investigation of the Effects of Polydopamine Nanoparticle Size on Their Antioxidant and Photothermal Properties: Implications for Biomedical Applications, ACS Appl. Nano Mater. 5 (2022) 1702–1713. https://doi.org/10.1021/acsanm.1c04536.

[81] G. Houthaeve, S.C. De Smedt, K. Braeckmans, W.H. De Vos, The cellular response to plasma membrane disruption for nanomaterial delivery, Nano Converg. 9 (2022) 6. https://doi.org/10.1186/s40580-022-00298-7.

[82] M. Zhang, Z. Ma, N. Selliah, G. Weiss, A. Genin, T.H. Finkel, R.Q. Cron, The impact of

Nucleofection® on the activation state of primary human CD4 T cells, J. Immunol. Methods. 408 (2014) 123–131. https://doi.org/10.1016/j.jim.2014.05.014.

[83] M. Schomaker, D. Killian, S. Willenbrock, D. Heinemann, S. Kalies, A. Ngezahayo, I. Nolte, T. Ripken, C. Junghanß, H. Meyer, H.M. Escobar, A. Heisterkamp, Biophysical effects in off-resonant gold nanoparticle mediated (GNOME) laser transfection of cell lines, primary- and stem cells using fs laser pulses, J. Biophotonics. 8 (2015) 646–658. https://doi.org/10.1002/jbio.201400065.

[84] L. Raes, C. Van Hecke, J. Michiels, S. Stremersch, J.C. Fraire, T. Brans, R. Xiong, S. De Smedt, L. Vandekerckhove, K. Raemdonck, K. Braeckmans, Gold Nanoparticle-Mediated Photoporation Enables Delivery of Macromolecules over a Wide Range of Molecular Weights in Human CD4+ T Cells, Crystals. 9 (2019) 411. https://doi.org/10.3390/cryst9080411.

[85] A.J. Jimenez, F. Perez, Plasma membrane repair: the adaptable cell life-insurance, Curr. Opin. Cell Biol. 47 (2017) 99–107. https://doi.org/10.1016/j.ceb.2017.03.011.

[86] Y. Zhen, M. Radulovic, M. Vietri, H. Stenmark, Sealing holes in cellular membranes, EMBO J. 40 (2021) 1–13. https://doi.org/10.15252/embj.2020106922.